NUCLEAR DEPENDENCE OF PROTON-INDUCED DRELL-YAN DIMUON
PRODUCTION AT 120GEV AT SEAQUEST

BY

BRYAN P. DANNOWITZ

DISSERTATION

Submitted in partial fulfillment of the requirements
for the degree of Doctor of Philosophy in Nuclear Physics
in the Graduate College of the
University of Illinois at Urbana-Champaign, 2016

Urbana, Illinois

Doctoral Committee:

Professor Jen-Chieh Peng, Chair
Professor Naomi C. R. Makins, Director of Research
Professor Michael Stone
Professor David Ceperley

Abstract

A measurement of the atomic mass dependence of Drell-Yan dimuons produced by 120GeV protons is presented here. Over 88,000 dimuon pairs with dimuon mass $M \geq 4.2\ GeV$ were recorded at SeaQuest from targets ^1H, ^2H, C, Fe, and W. The ratio of dimuon yield per nucleon for heavy nuclei versus ^2H, $R = Y_A/Y_{^2H}$, is sensitive to modifications in the anti-quark sea in nuclei for the case of proton-induced Drell-Yan. No nuclear modifications are observed over the target quark momentum fraction range $0.1 \leq x_t \leq 0.45$. These results are compared to predictions of models of the EMC effect.

To my dog, Charlemagne.

Acknowledgments

This paper does not acknowledge Star Wars Episodes I-III, nor does it acknowledge Pluto as a full-on planet.

Table of Contents

List of Tables

List of Figures

List of Abbreviations

ACNET	Accelerator control system network
AD	Accelerator division (of Fermilab)
BIM	Beam intensity monitor
BOS	Beginning of spill
BPM	Beam profile monitor
CEBAF	Continuous Electron Beam Accelerator Facility
CODA	CEBAF On-line Data Acquisition
DAQ	Data acquisition
DC	Drift chamber
DIS	Deep-inelastic scattering
DY	Drell-Yan
E906	Experiment number 906 at Fermilab National Accelerator Laboratory, a.k.a. SeaQuest
EOS	End of spill
EPICS	Experimental physics and industrial control system
FEE	Front-end electronics
FNAL	Fermi National Accelerator Laboratory (Fermilab)
FPGA	Field programmable gate arrays
IC	Ion chamber
KTeV	Fermilab experiment that previously inhabited the NM4 experimental hall
LINAC	Fermilab Linear Accelerator
LO	Leading order
MI	(Fermilab) Main Injector
MOSFET	Metaloxidesemiconductor field-effect transistor
NDF	Neutral density filter
NLO	Next-to-leading order

NM	Neutrino-muon beam line
NNLO	Next-to-next-to-leading order
PDF	Parton distribution function
PID	Particle identification
PMT	Photomultiplier tube
RF	Radio frequency
RFQ	Radio frequency quadrupole
ROC	Readout controller
SEM	Secondary emission monitor
TS	Trigger supervisor
QCD	Quantum chromodynamics
QED	Quantum electrodynamics
QIE	Charge (Q) integrator and encoder
RDBMS	Relational database management system
SQL	Structured querying language
SWIC	Segmented wire ion chamber
VME	Versa Module Europa

List of Symbols

μ^+	Positive muon
μ^-	Negative muon
J/Ψ	The first excited state of a *charm-anticharm* meson family

Chapter 1

Introduction

Chapter 2

Nucleon Internal Structure Phenomenology

The topic of this paper, simply put, is the exploration of the momentum structure of the *nucleon*, a particle that makes up an atom's nucleus which can be either a proton (p) or a neutron (n). By momentum structure, I refer to the fractional momentum distributions carried by the nucleon's constituent particles, quarks and gluons.

While a complete review of the history and physics behind nucleon structure and its investigative probes is beyond the scope of this paper, a brief overview of deep-inelastic scattering and Drell-Yan will help in understanding concepts and terminology relevant to this and later chapters.

2.1 Introduction

The first indication that the proton may have some internal structure was in a 1933 experiment by Estermann *et al.* measuring the magnetic moment of the proton [6]. Since the proton was thought to be a point-like Dirac particle, it's magnetic moment (μ_p) was expected to be $\mu_p = \frac{e}{2m_p} = 1n.m.$, or one *nuclear magneton*. The experiment resulted in a value of 2.5 n.m., leading many to reconsider the notion that the proton is indeed point-like.

Around the same time, Hideku Yukawa is credited for establishing the first theory of a *strong force*, a force binding together nucleons in a nuclei against the sizable *Coulomb* repulsion of protons []. The force was theorized to be mediated by the exchange of particles called *mesons*, and its range was limited to nuclei-scale distances, seeing as it's not observed at larger distances. Based upon the size of the nucleus, Yukawa estimated the mass of the intermediating particles to be approximately $2 \times 10^2 m_e \approx 100MeV$, where m_e is the electron mass. The following year, Anderson et al. discovered the muon (μ) at around this mass [], which confused many, as it did not seem to partake in strong interactions. Eventually, by 1947, the meson theory was validated by the discovery of the *pion* by Powell *et al.* [], and Yukawa was awarded a Nobel Prize for his theory in 1949.

While the

The study of nucleon structure has come a long way, and at present, the proton is described as a composite particle consisting of three point-like *valence quarks* interacting with each other through exchange of gluons.

2.2 *ep* Scattering

Nucleon structure is still today one of the great frontiers of nuclear physics. The primary tool used to probe the parton distribution has been Deep Inelastic Scattering (DIS), which is the scattering of a charged lepton off of a nucleus by the exchange of a virtual photon. As the energy of the exchanged photon increases, the scattering becomes inelastic and is able to resolve the partonic substructure of hadrons.

2.3 The Drell-Yan Process

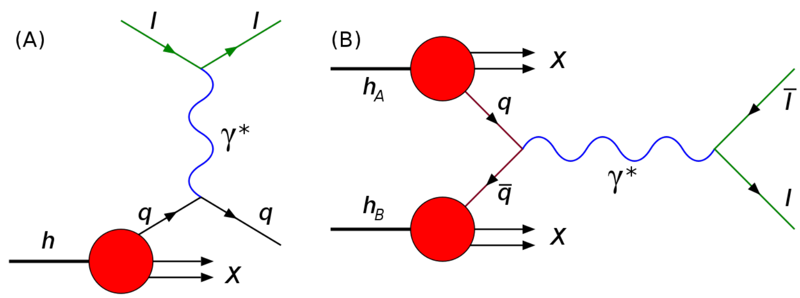

Figure 2.1: (A) Deep inelastic scattering (DIS) is a t-channel interaction which uses the emission of a virtual photon to probe the target hadron. (B) The similar Drell-Yan (DY) process, using the s channel version of the DIS interaction, via annihilation of a beam quark with an anti-quark from the target hadron.

As useful as this has been, DIS is only sensitive to momentum and charge of the partonic structure.

In 1970, S. Drell and T.M. Yan were the first to study the process in which high-mass lepton production occurs as a result of inelastic hadron-hadron collisions [4]. This so-called "Drell-Yan" (DY) process is identified to be the result of a quark-antiquark annihilation into a virtual photon which then decays into a lepton pair.

This process, as you see in Figure 2.1, is the s-channel counterpart to DIS's t-channel process. Similarly Drell-Yan can give a complementary view of the nucleon's parton distribution. The differential cross section that we will be using is in terms of the fractional momentum variables, x_1 and x_2, which represent the fraction of the respective hadron's momentum carried by the beam quark and target anti-quark, respectively.

To begin, we start with the annihilation cross section for $e^+e^- \to \mu^+\mu^-$ and simply add a color factor of $\frac{1}{3}$ since only like flavor-antiflavor quarks will annihilate, and use the charge e_i^2 for quark flavor i [5]. Other variables referred to in Eq 2.1 and 2.2 and more are defined in Table 2.1.

$$\frac{d\hat{\sigma}}{dM} = \frac{8\pi\alpha^2}{9M} e_i^2 \delta(\hat{s} - M^2) \tag{2.1}$$

The hadronic Drell-Yan differential cross section can be obtained from this by the convolution of the above cross section with the quark distributions in the beam and target.

$$\frac{d^2\sigma^{DY}}{dx_1 x_2} = \frac{8\pi\alpha^2}{9sx_1x_2K(x_1,x_2)} \sum_i e_i^2 [q_i^b(x_1)\bar{q}_i^t(x_2) + \bar{q}_i^b(x_1)q_i^t(x_2)] \tag{2.2}$$

Variable	Description
α	The fine structure constant
$K(x_1, x_2)$	High-order QCD correction term
$\sqrt{s}$	The center of mass energy of the hadronic collision
$\sqrt{\hat{s}}$	The center of mass energy of the $q\bar{q}$ collision
Q^2	The four-momentum of the intermediate time-like photon, squared
$q_i^{t/b}(x)$	The quark number density in the nucleon of the target/beam

Table 2.1: Kinematic variables relevant to the Drell-Yan process .

In addition to the leading-order DY term, there are high-order QCD corrections to consider. These have been studied and accounted for up to $O(\alpha_s)$ and $O(\alpha_s^2)$. These include contributions from high-order $q\bar{q}$ annihilation ($q\bar{q} \to \gamma * +g$) and gluon Compton scattering ($q + g \to \gamma * +q$) as seen in Figure 2.2 [5]. The cumulative effect is denoted in the cross section as the $K(x_1, x_2)$ factor, which can vary between 1.6 and 2.8. For our x_1 and x_2 range, $K \sim 1.6$.

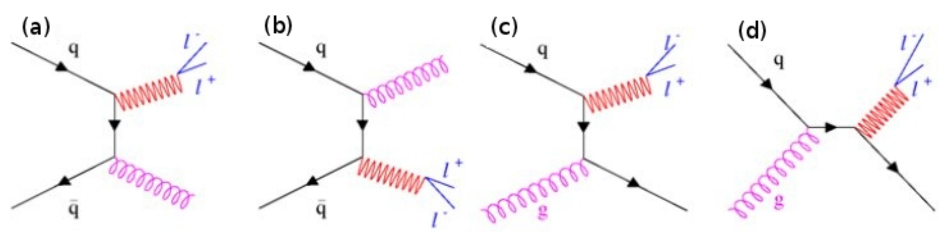

Figure 2.2: The Drell-Yan process has a large range of higher-order QCD corrections that need to be accounted for. (A) and (B) are high order $q\bar{q}$ annihilations, and (C) and (D) are gluon "Compton scattering" terms.

Now the question is: what can the Drell-Yan process tell us that the well-exercised DIS scattering cannot? The core answer to that is that DIS is not intrinsically sensitive to flavor, whereas DY is. However, to answer the question fully, we must discuss the distribution of quarks in a nucleon.

Let's say that we have two hadrons A and B colliding; a parton of type a (u, d, s, g, etc.) comes from A and carries with it a fraction of A's momentum (x_A). The same goes for hadron B; a parton of type b comes

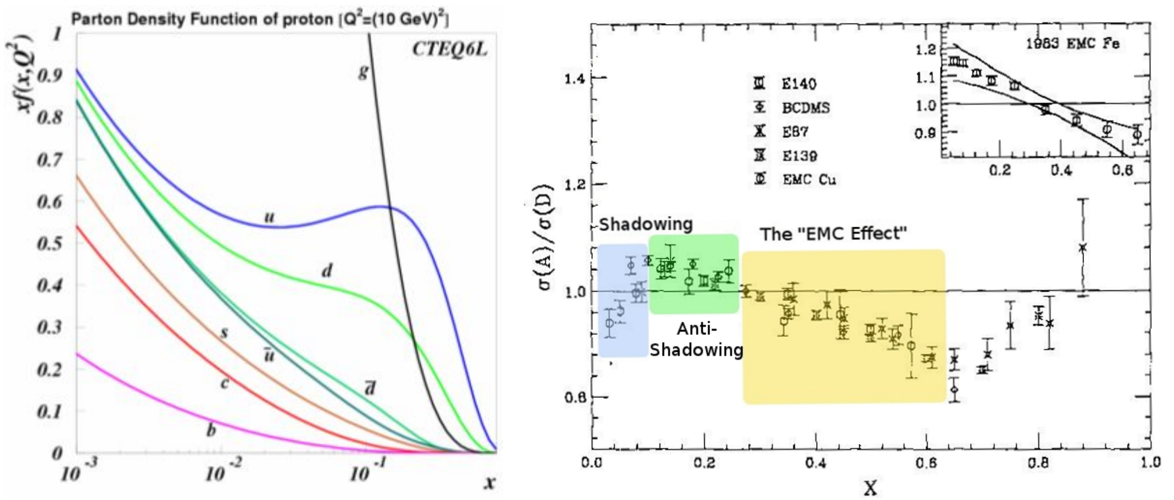

(a) The parton distribution function describing the momentum carried by different types of quark in the proton.

(b) The ratio of cross sections (per nucleon) as a function of the target's fractional momentum, x_2. The EMC Effect region, $0.3 < x_2 < 0.6$ is the phenomenon discussed here.

Figure 2.3: The proton's momentum distribution and the EMC Effect, with key regions highlighted.

from B and carries momentum fraction x_B. Now, the probability of finding the discussed parton from A is given by $f_{a/A}(x_A)dx_A$. Likewise, the probability of finding the discussed parton from B is $f_{b/B}(x_B)dx_B$.

These *structure functions*, $f_{a/A}(x)$ are called the *parton distribution functions* (PDF's), and they have been the focus of a great deal of experiments over the years by several collaborations. Due to the complex nature of lattice QCD, these PDF's are determined empirically, with only a few rules based in theory. It is important to note that there is normally a Q^2 dependence of these PDF's. At high enough Q^2, as it is in the case of our experiment, the PDF's no longer scale with Q^2 [16]. That is, for a given x, the PDF is independent of Q^2.

An important metric to observe is the probability that a parton a carries a momentum fraction x_A in its hadron A. This can be represented by the following expression: $x_A f_{a/A}(x_A)dx_A$. For Drell-Yan interactions in the study proposed here, we are interested in the momentum distribution amongst the quarks in the proton. The CTEQ collaboration has collected data from many experiments, yielding the model represented in Figure 2.3a [15].

Looking to Figure 2.3a we see that at $x > 0.1$, u and d quarks dominate $\bar{u}$ and $\bar{d}$ quarks. This is key, because this means that, for SeaQuest where we have high x_1 and lower x_2, the Drell-Yan process is probabilistically dominated by a quark from the beam annihilating with an antiquark from the target. All antiquarks that exist in the target nucleons must come from what are called the *sea quarks*, or the virtual $q\bar{q}$ pairs that pop in and out of existence amongst the gluons and valence quarks.

As we will discuss in the next section, partons in a bound nucleon behave differently than partons in a free nucleon. By studying Drell-Yan in nuclear targets, we can investigate the degree to which this modification is the result of a modification to the quark sea.

2.3.1 The Drell-Yan Cross-Section

2.3.2 Drell-Yan Kinematics

2.4 The EMC Effect

The European Muon Collaboration, in 1983, measured the DIS cross section per nucleon ratios of Fe to D over a large kinematic range. The result, as seen in the top right of Figure 2.3b came as quite a surprise. It was revealed that the structure function of a nucleon bound in a nucleus differs fundamentally from that of a free nucleon [2]. This difference was not a simple or small effect either; the cross section per nucleon of a nucleus showed to be smaller than that of deuterium at very low x_2, greater than deuterium at $0.1 < x_2 < 0.2$, and then steadily less than deuterium for $0.2 < x_2 < 0.6$.

This complex, unexplained behavior opened up a new field of research and theoretical work. Following suit, the different aspects of this nuclear modification garnered some common nicknames. The region where $x_2 < 0.1$ became known as *"Nuclear Shadowing"*, the transition region of $0.1 < x_2 < 0.2$ is known as *"Anti-shadowing"*, and the linear decline in the ratio of cross sections between $0.2 < x_2 < 0.6$ is generally referred to as the *"EMC Effect"* [7].

The phenomenon was simple – DIS off of a bound nucleon was not the same as off of a free nucleon – but hundreds of theoretical papers were written attempting to explain it away, from multiquark ($6q$) clusters to the exchange of virtual pions in the nucleus. Some have joked that EMC should stand for *"Every Model is Cool"*. The focus of recent work (and this paper) is on the "EMC Effect" region, characterized by the distinctly linear downward slope.

Recent experiments at Hall C at JLab and SLAC suggest the following regarding the EMC Effect [16]:

- It is Q^2-independent
- It's x-dependent shape is universal (across various nuclei)
- The magnitude (slope) of the effect varies with A
- It thereby might be related to nuclear density

In parallel to this effort, many researchers were working on high-momentum nucleons and short range correlations (SRC's), neither aware yet of their common ground.

Chapter 3

Apparatus

SeaQuest is the operational name of Fermilab Experiment #906 (*E-906*) performed at its Neutrino-Muon (*NM*) experimental area. The experiment was designed to take *high-intensity beam* at relatively *low center-of-mass energy*, provide *good mass resolution*, and allow for *accurate target-to-target systematic normalization.* The apparatus consists of a moving target table, two dipole magnets, 8 hodoscope planes, 24 drift chamber planes, and 4 proportional tube planes. Upstream of the target table (towards the beam source), there is also a Čerenkov counter for beam intensity monitoring and there are several segmented wire ionization chambers (SWIC's) for beam profiling.

3.1 Apparatus Overview

SeaQuest is a fixed-target experiment. In this style of experiment, a stationary target is placed in the path of an accelerated beam of particles, as opposed to *collider* experiments where two accelerated beams are directed against each other, in opposite directions. The proton beam interacts with the target material and produces a variety of daughter particles. These daughter particles are tracked through a forward spectrometer and selectively filtered dependent on the purpose of the study.

The tuned and monitored 120 GeV proton beam is sent from the Fermilab Main Injector (MI) where the beam protons strike one of the 7 targets. The high-momentum charged particles that are produced are focused onto the various detectors with the solid iron dipole magnet, FMAG, or NM3S. This solid focusing magnet also sweeps away low-momentum particles and acts as a beam dump / absorber.

The SeaQuest Spectrometer (Fig. 3.1) consists of a focusing magnet to bend charged particles into the experiment's acceptance, several tracking chambers that record the positions of charged particles through the length of the spectrometer, and an analyzer magnet to bend the particles between tracking stations. The spectrometer measures particle momenta by recording the bend of each charged particle as it passed through the analyzer magnet, where the magnetic field is known. This is performed by reconstructing the trajectory of a particle in one half of the spectrometer (before the analyzer magnet) and then similarly

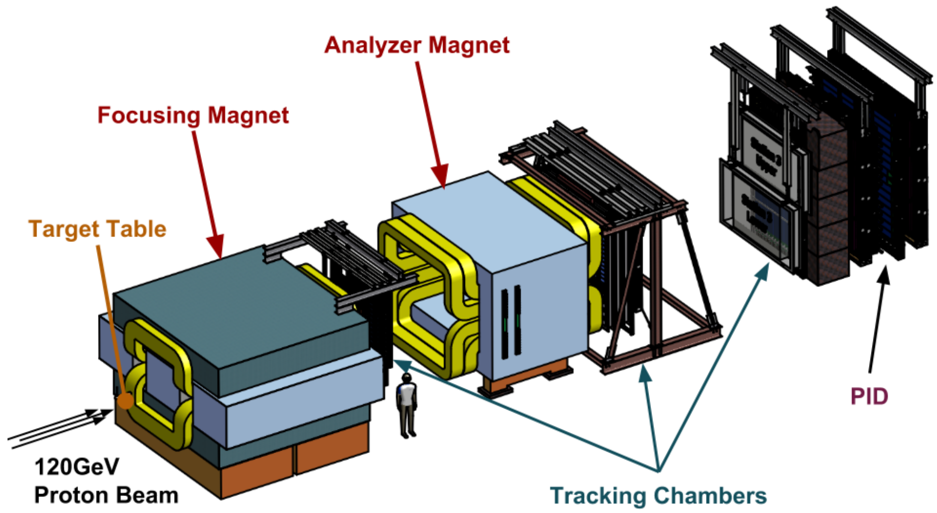

Figure 3.1: Perspective view of the SeaQuest spectrometer apparatus.

reconstructing the trajectory of particles in the other half. If two trajectories can be matched up, then the particle momentum can be extracted by taking the ratio of the magnet's p_T-kick to the change in the track's direction.

The spectrometer geometric design and event triggering selection is optimized to detect oppositely-charged pairs of muons while minimizing the sensitivity to various sources of unwanted backgrounds. Positive identification of muons is achieved by requiring signals in the hodoscopes for known muon *"roads"* along with requiring signals in the proportional tubes located at the farthest end of the experiment, past an iron wall. Electrons and any hadrons are stopped by the solid iron focusing magnet an iron wall further down, while muons will pass through them unencumbered.

The coordinate system is defined as the following: the z-axis points along the beam direction, the y-axis points upwards vertically, and the x-axis lies along the horizontal direction in such a way that a right-handed coordinate system is formed. The terms *upstream* and *downstream* are often used when referring directions or regions in the experimental hall. *Upstream* often refers to the region of the experiment towards the beam source, while *downstream* refers to everything towards the $+z$ direction. The The origin of the coordinate system was chosen to be the point where the proton beam meets the *upstream*-facing surface of FMAG, the solid focusing magnet.

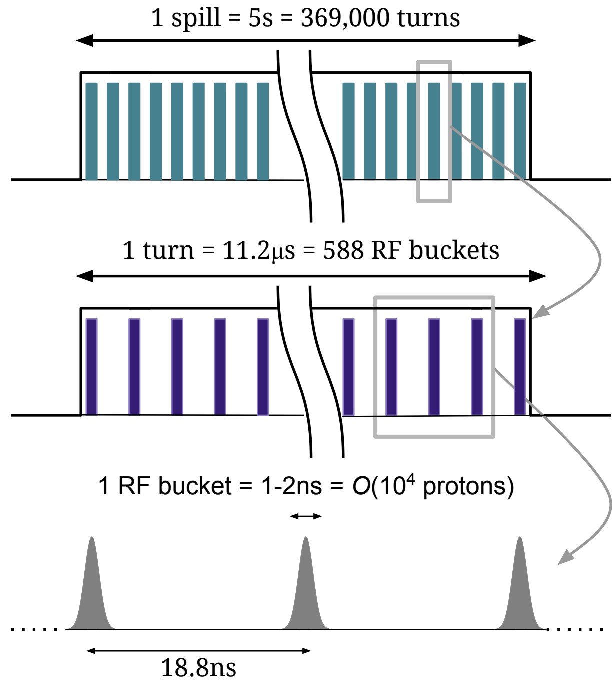

Figure 3.2: Spill structure of the beam delivered to SeaQuest.

3.2 Main Injector Proton Beam

The Fermilab Main Injector (MI) receives protons that have been accelerated by the Radio Frequency Quadrupoles (RFQ), the Linear Accelerator (LINAC), and the Booster, and it continues to accelerate them from 8 GeV up to the nominal energy of 120 GeV. Along the way, the radio-frequency cavity (RFC) accelerators in the LINAC and the MI "bunches" up the protons such that the beam has its characteristic 53.1 MHz structure. After the period of acceleration, the protons are then 'scraped off' slowly with each passing *turn* of the collected proton beam and sent down the Neutrino-Muon (NM) beam delivery line for approximately five seconds of every minute, called a "slow spill", or just "spill". Beam is extracted using a resonant process, and the extracted beam retains the 53.1 MHz structure of the Main Injector RFC. Each bunch, or "bucket" of protons is less than 2 ns long and the time between bunches is approximately 18.8ns. The spill structure of the beam is depicted in greater detail in Figure 3.2.

The beam sent to SeaQuest is not uniform in time throughout the spill (in more ways than one). There are beam bunches in the MI that are intentionally left empty so that the abort kickers can ramp to full field during a gap in the beam. There are also bunches left empty to allow the injection kickers to inject 8 GeV protons from the Booster without disturbing bunches of protons already in the Main Injector. Typically, 498 of the 588 "RF buckets" in the Main Injector contain protons during the SeaQuest slow spill cycle. It

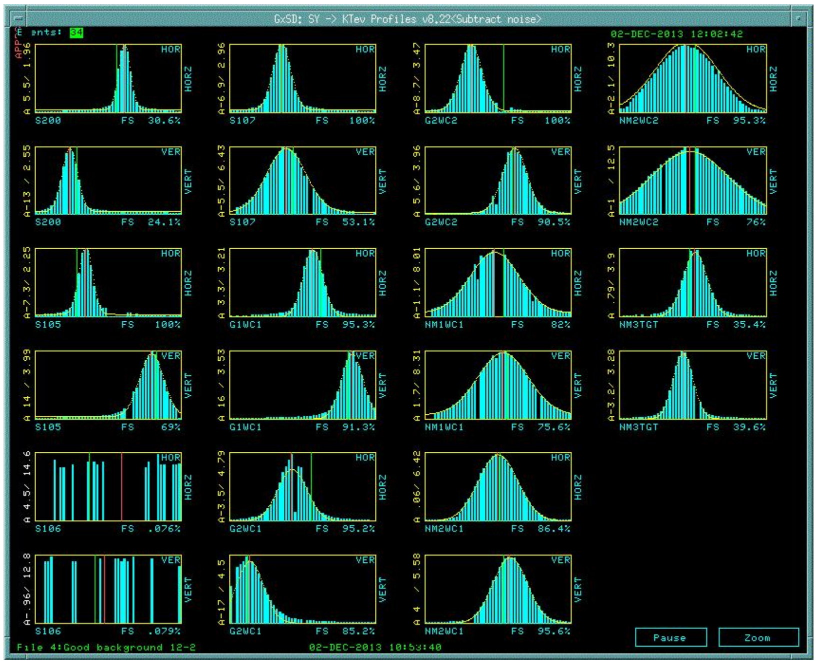

Figure 3.3: Beam profile detailed by SWIC detectors along the NM beam line.

is the case, however, for SeaQuest, that the intensity of the bunches corresponding to these 498 full buckets varies greatly throughout the slow spill. On *average*, each bucket will have $O(10^4)$ protons, and the spill has an intensity of approximately 2×10^{12} protons per second and therefore about 1×10^{13} protons delivered per spill.

Several guiding and focusing magnets bend and deliver beam to the NM beamline which serves both the test beam facility and SeaQuest at NM4. The beam is focused to a width of 250μm. The profile, position, and intensity are measured along the NM beamline by several detectors. The intensity of the beam is monitored by an ion chamber (IC) and a secondary emission monitor (SEM) in the NM3 sector. The beam profile and position are monitored by SWICs and beam-position monitors (BPMs), respectively. The Accelerator Control Network (ACNET) display of the SWIC readout can be seen in Figure 3.3. The closest BPMs and SWICs to the spectrometer were located in NM2 enclosure. The beam profile does not maintain its 250μm shape, and spreads slightly as it moves towards the spectrometer. The final beam profile is measured by inspecting the upstream-facing side of the solid targets, and it was found to be approximately 6mm wide by 1mm high.

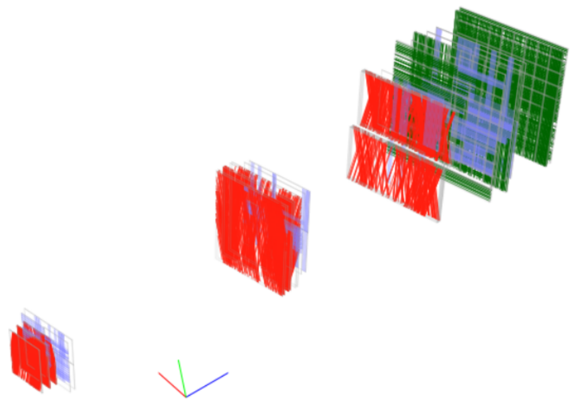

Figure 3.4: A single high-intensity event with majority of all detector elements firing off. White space within the rectangles indicates inactive elements whereas red, blue, and green represent elements which have fired during that event. Track reconstruction in these cases is impossible.

3.3 Beam Intensity Monitor

SeaQuest's trigger system (described in detail later) mostly fires on fake dimuons caused by two low p_T muons from unrelated pion decays. The hits in downstream hodoscopes from the pions combined with hits in the upstream hodoscope from two other unrelated particles frequently add up to a false dimuon signal. Since this type of fake trigger involves four unrelated particles, the probability that a trigger will occur increases with I^4, where I is the intensity of the beam bucket, or the number of protons in the triggered beam bunch.

The SeaQuest data acquisition system (also described later in detail) can read out approximately 3000 events per second without significant dead time. During the commissioning run of SeaQuest, the trigger rate was very high and the trigger dead time was close to 100%. These triggers were taken at such high beam intensities that the occupancy of all SeaQuest detector elements was more than 50%, making pattern recognition essentially impossible (see Figure. 3.4). The Beam Intensity Monitor (BIM) was designed to solve this problem.

The SeaQuest Beam Intensity Monitor (BIM) senses when the beam intensity is above a programmable threshold. If an RF bucket with an intensity above this threshold is detected, the BIM sends a signal to inhibit certain triggers until the intensity once more falls below the threshold. The inhibit threshold is tuned frequently as trigger and beam conditions change, but the inhibit threshold is typically set at approximately 95,000 protons per RF bunch. For reference, a full RF bucket at an intensity of 2×10^{12} protons per spill is $\approx$10,000 protons.

The beam intensity is measured using an atmospheric pressure gas Čerenkov counter. A gas mixture

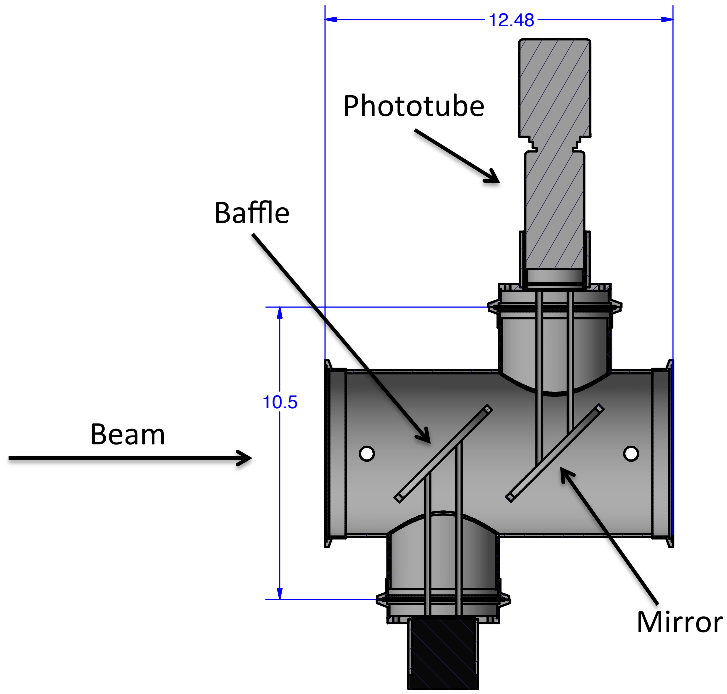

Figure 3.5: The Beam Intensity Monitor (BIM) Čerenkov counter. Measurements are in inches.

of 80% Argon and 20% CO_2 is used as the Čerenkov radiator. The counter and readout electronics were designed to have $O(ns)$ time resolution, and a linear response over a large dynamic range. A diagram of the counter is shown in Figure 3.5. A 45 degree aluminized Kapton mirror directs light to a single photomultiplier tube. A *baffle* of black construction paper held parallel to the mirror ensures that the proton path length through the light-radiating gas with respect to the mirror is independent of beam position. A two-inch diameter 8-stage photomultiplier tube (PMT) is positioned close to the mirror so that all Čerenkov light created between the baffle and the mirror falls directly on the aperture of the PMT. It was observed during the commissioning run that after exposure to $\approx 3 \times 10^{17}$ protons (3 weeks of uninterrupted usage), the mirror reflectivity is significantly reduced in the beam spot, and the mirror then needs to be replaced.

The signal from the BIM is integrated and digitized using a custom charge (Q) integrator and encoder (QIE) integrated circuit board, which comes from a family of circuits used first by the KTeV experiment at Fermilab[19]. The chip is clocked with the Main Injector RF clock and provides an ADC (analog-digital conversion) every 18.8ns clock cycle. The light incident on the photomultiplier tube is attenuated using neutral density filters (NDF's) so that the QIE least count corresponds to ∼30 protons per beam bunch.

In addition to inhibiting triggers during high-intensity periods of beam, the BIM readout module also provides critical information used to calculate the number of protons incident on the SeaQuest targets while the experiment is ready and able to trigger. This value is needed to normalize SeaQuest cross section measurements. The BIM readout module provides the following:

- Sum of all ADC signals for the entire spill (QIESum).
- Sum while inhibit is asserted at trigger logic.
- Sum during trigger dead time.
- A snapshot of beam intensity 16 buckets before and after the triggered RF bucket

These are used to calculate a ratio of protons that were 'live' (the experiment can trigger) via the following:

$$liveRatio = \frac{QIESum - (inhibit\ sum + dead\ time\ sum)}{QIESum} \tag{3.1}$$

$$liveProton = totalProton \cdot liveRatio \tag{3.2}$$

where "totalProton" is the intensity value recorded from the SEM detector located just upstream of the BIM Čerenkov counter. The SEM itself is calibrated by foil activation. The snapshot of the triggered RF bucket intensity along with the 32 surrounding RF bucket intensities is used for studies and corrections of the rate-dependent effects on detector efficiencies and reconstructed measurements.

3.4 The SeaQuest Targets

A wide range of atomic weights (from 2 to 184) is required to do an A-dependence study of the Drell-Yan process. At SeaQuest, the targets used are ${}^1H(\ell)$, ${}^2H(\ell)$, C, Fe, and W. In addition to the two liquid targets and the three solid targets, two positions on the target table were used for measuring background signal rates: an empty flask, identical to the flasks used for the ${}^1H$ and ${}^2H$ targets, and a single empty solid target holder. Colloquially speaking: the ${}^1H$ target is interchangeably referred to as the liquid hydrogen target, ℓH_2, *LH2*, or H_2; ${}^2H$ is likewise referred to as the liquid deuterium target, ℓD_2, *LD2*, or D_2; the empty flask is referred to as the "Empty" target; the empty solid target holder is referred to as the "None" target.

These are all mounted on a laterally-moving, remotely positionable table (in the $\pm x$ direction), able to move over a range of 91.4cm. The table's center is located at $(0, 0, -1.25)$ meters, directly in front of the upstream face of FMAG, the solid iron focusing magnet. Because of the ∼5.0cm diameter of the targets and

Position	Material	Density [g/cm^3]	Thickness [cm]	Interaction Length	Spills/ Cycle (%spills)
1	H_2	0.07065	50.8	0.06902	10 (43%)
2	Empty	NA	NA	0.0016	2 (9%)
3	D_2	0.1617	50.8	0.1144	5 (22%)
4	None	NA	NA	0.0	2 (9%)
5	Iron	7.874	1.905	0.1135	1 (4%)
6	Carbon	1.802	3.322	0.0697	2 (9%)
7	Tungsten	19.30	0.953	0.0958	1 (4%)

Table 3.1: Characteristics of the seven SeaQuest target positions. The "Spills/Cycle" is only a typical configuration and can vary according to needs and running configurations. The non-zero interaction length of the empty flask is due to the 51μm-thick stainless steel end-caps of the flask and the 140 μm-thick titanium windows of the vacuum vessel that contains it.

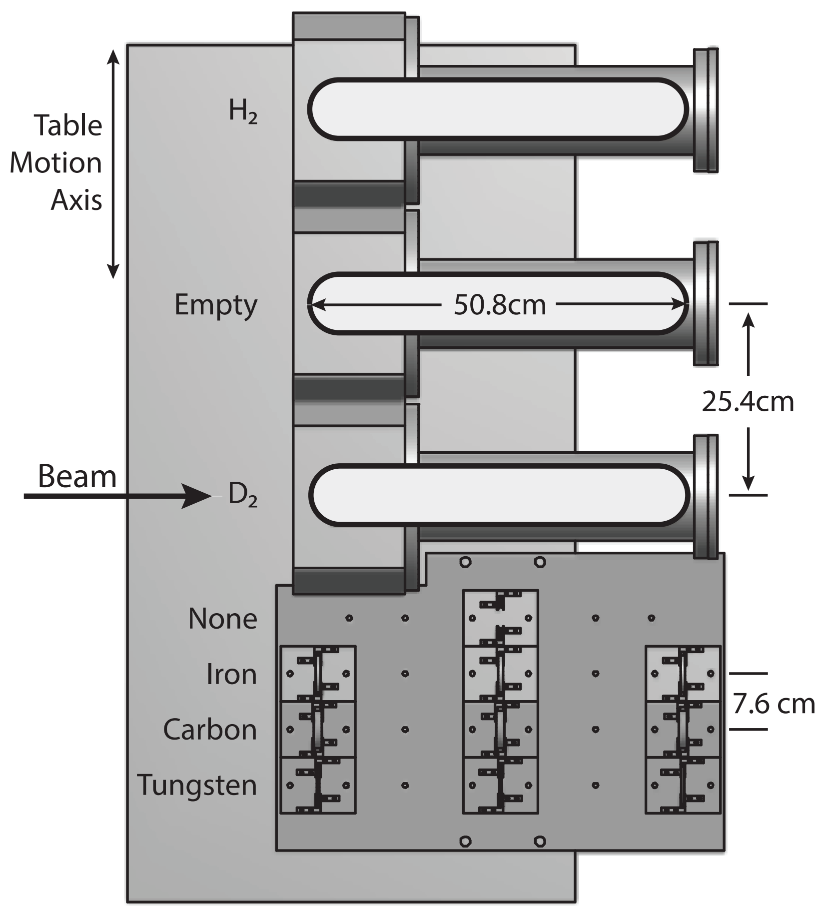

Figure 3.6: The layout of the target table and its seven target positions, as seen from above.

the 6x1mm dimensions of the beam, the targeting efficiency was 100%. The details of the target materials are summarized in Table 3.1, and the layout of the target table can be seen in 3.6.

The H_2 gas used is "Ultra High Purity 5.0 Grade" or 99.999% pure. The deuterium has come from two different sources. The first of these is Fermilab-provided supply of gas left over from previous bubble chamber experiments. This gas was known to have a small hydrogen contamination and was measured by mass spectroscopy to have a composition of 85.2% D_2, 12.7% HD, 1.2% ^4He, and 0.8% H_2 by mole. As analysis of experimental data commenced, handling the ramifications of the D_2 impurity came under focus. Unexpected bottle-to-bottle variation in contamination became evident, and the sample-taking methodology itself for spectroscopy became suspect of introducing contamination. In order to no simplify analysis and reduce the substantial complexity and cost of further gas analysis, SeaQuest switched to commercially available "Research Grade" D_2, which is better than 99.6% pure with virtually all HD to balance. The data analyzed in this paper deals with the impure D_2 target material before this switch. Further information on the D_2 composition and how it is handled in analysis will be covered in Chapter 4.

Each of the three solid target positions is divided into three disks of 1/3 the total thickness provided in Table 3.1. These disks are spaced 25.4cm apart to approximate the distribution of the liquid target, thereby minimizing target-dependent variation in spectrometer acceptance. The one exception to this is that during the Run II period the iron plugs were more closely spaced (17.1cm). The decision to place these iron disks closer together than the rest during Run II is still unclear.

The target table is able to move between two different targets in about 30 seconds. This allows a change in target in the 55 seconds between successive spills. With this frequent target interchange, the systematic uncertainties associated with drifts in beam characteristics, monitor gains, and detector efficiencies are reduced to a minimum when investigating A-dependent ratios. How much beam time each target received is determined by interaction lengths of the targets along with the amount of statistics desired for certain targets. As the flagship measurement of SeaQuest is the $\bar{d}/\bar{u}$ asymmetry, more emphasis was placed on the hydrogen and deuterium than the nuclear targets. The spills per cycle and beam time allocation can be found in Table 3.1.

3.5 Focusing and Analyzing Magnets

Two large dipole magnets are used in the experiment to be select forward going ($x_F > 0$) dimuons, reject low-momentum particles, and analyze their kinematic characteristics. The most upstream magnet, denoted "FMAG", is a solid iron A-frame magnet with an aperture of 1.22m in the x-direction and 66cm in the

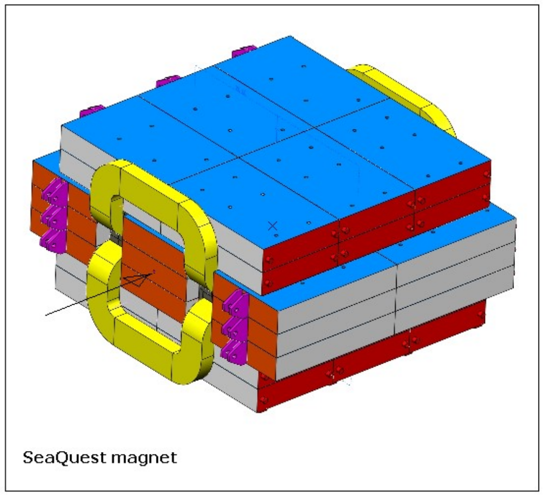

Figure 3.7: Perspective drawing of FMAG's aluminum coils embedded in an arrangement of iron slabs.

y-direction. It is assembled from 43.2cm x 160cm x 503cm iron slabs, as shown in Fig. 3.7. The magnet has no air gap, and the iron has extremely high purity, allowing a 2000A excitation current to generate a nearly constant, central magnetic field of 1.9 Tesla (yielding a 2.91 GeV/c total magnetic deflection). The field is generated by exciting the embedded aluminum *"bedstead"* coil to 2000 Amps at 25 Volts (50 kW). The current exciting FMAG is monitored by the Fermilab ACNET system and is broadcast to the SeaQuest slow data acquisition system every acceleration cycle. The excitation is also input to the beam-disabling safety system in order to prevent beam from hitting the SeaQuest spectrometer when FMAG is not fully powered. FMAG also acts as the beam dump for the 120 GeV beam. There is a 5cm diameter by 25cm deep bore drilled into the upstream end of FMAG (recall, this is the origin of the experiment's coordinate system). The 120 GeV protons that do not interact in the SeaQuest targets 125cm upstream of FMag, interact in the central iron slab. Most of the 2.0 kW beam power is dissipated in this slab and is eventually conducted to the coils and external surfaces to be radiated away.

The downstream magnet, denoted "KMAG", is a 300cm long iron rectangular magnet with a 289cm wide by 203cm high central air gap. It was originally constructed by the KTeV collaboration [1] at Fermilab. It is excited to a central field of 0.4 Tesla (0.402 GeV/c magnetic deflection) by 1600 Amps at 270 Volts (430kW). The spatial distribution of the magnetic field in KMAG was measured by the KTeV group and re-verified by SeaQuest. In normal running conditions, both FMag and KMAG bend muons horizontally in the same direction. This two-magnet configuration is often referred to as a focusing spectrometer.

The 2.91 GeV/c and 0.402 GeV/c magnetic deflection delivers a transverse-momentum (p_T) kick along the to charged particles passing through the spectrometer. The magnets bend the paths of the muon in the $\pm x$ direction, with the sign depending on the orientation of the magnetic fields and the particles' charges.

Between Run II and Run III of data taking, the current direction was reversed, thereby reversing the direction of the magnetic fields. During Run II, the magnetic fields were pointing in the $-y$ direction, and in Run III, the magnetic fields were flipped to point in the $+y$ direction. This was done for two reasons: (1) to identify any left-right asymmetries in the experiment, and (2) to limit the amount of radiation on the electronics in the experimental hall, as the large amount of positive particles were being swept directly towards the electronics racks during Run II.

3.6 Beam Dump, Shields, and Absorbers

In order to prevent damage to the downstream detectors from the beam and reduce signals from incidental radiation, the spectrometer is designed with a beam dump and two hadron absorber walls. Approximately 125cm downstream of the target table is the water-cooled beam dump whose upstream face is located at $(0.0, 0.0, 0.0)$ m. The beam dump is one of the many solid iron 5m blocks that fill and surround the FMAG coils. The whole length of the beam dump along the beam axis is equivalent to ≈ 35 nuclear interaction lengths of iron.

Between the downstream face of FMAG and Station 1, there is a 2 cm thick wall of borated polyethylene which is put in place as a fast neutron shield. This material is 5% boron by weight, with the rest being polyethylene. The polyethylene contains high hydrogen content, making it an effective fast neutron radiation shield, slowing down the fast neutrons down to thermal speeds. The boron in the material provides attenuation of thermal neutrons, thus reducing the levels of capture-gamma radiation elsewhere in the experiment. Borated polyethylene at this thickness is a common and optimal neutron shielding material for areas of low to intermediate neutron flux where the temperature is below 82°C [*citation needed*]. These conditions make the downstream side of FMAG ideal for its placement.

Farther downstream, there is another hadron absorber wall located between Station 3 and Station 4. The absorber wall consists of a stack ot 98cm thick iron blocks. This is an equivalent of ≈ 6 nuclear interaction lengths. The purpose of this wall is to identify muons at the rear of the apparatus by effectively blocking all other types of particles. The only charged particles which can penetrate this absorber wall are muons.

3.7 Tracking Detectors

The tracking detectors are the instruments used for measuring the values of the kinematic variables of the dimuon pairs. Several different types of detectors are grouped together to form a detector *Station*. The types of detectors used are hodoscopes, wire chambers, and proportional tubes. There are four stations throughout

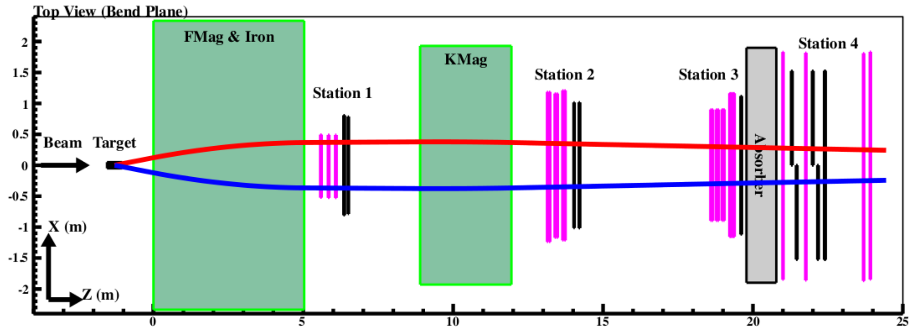

Figure 3.8: Spectrometer layout of FMAG, KMAG, and Detector Stations 1-4.

the experimental hall that provide tracking information at different points along the spectrometer, numbered from 1 to 4 in order of increasing z. Station 1 is located between FMAG and KMAG. Station 2 is located at the downstream face of KMAG. Station 3 and 4 are just upstream and downstream, respectively, of the iron absorber wall. The Station layout can be seen in Fig. 3.8

3.7.1 Triggering Hodoscopes

Hodoscope arrays are located at each of the four detector stations. These detectors' primary usage is to select events with two opposite-signed muon tracks in them. Certain 'roads' through the spectrometer are defined in the fast trigger logic, and when two desired roads are observed in a given event, the trigger system tells the data acquisition systems to record that event's data. In addition to this, the hodoscopes provide analysts with the ability to discard or ignore certain hits in adjacent chambers for which there is no corresponding nearby hodoscope hit. This is useful in decreasing the hit multiplicities in the wire chambers, which in turn decreases the combinatoric complexity of reconstruction algorithms.

Each of the eight hodoscope planes are split into two halves: top and bottom in the case of planes with vertically-oriented paddles, or left and right for planes with horizontally-oriented paddles (denoted by 'T', 'B', 'L', and 'R', respectively). In each half-plane, the hodoscopes are a set of long rectangles arranged 'picket fence'-style with a small 0.3175cm overlap, as to prevent any particles from possibly slipping between paddles. A single hodoscope detector element is composed of plastic scintillator material connected to Philips XP 2008 photomultiplier tubes (PMT) by plexiglass light guides. Stations 1, 2, and 4 each have two hodoscope planes, with planes of both vertically- and horizontally-oriented paddles (for measuring in x and y, respectively). Station 3 only has vertically-oriented plane, and thus measures in the $x-$direction only, which is in the experiment's $x-z$ bend plane. The hodoscope planes are named according to detector station and the direction that they measure. For example, the y-measuring hodoscope plane in Station 2 is called

"H2Y". The individual half-planes are named according to detector station and which half it is of the two. For example, the top half of the x-measuring hodoscope plane in Station 1 is referred to as "H1T". As such, the "H3X" detector is composed of "H3T" and "H3B". The detailed specifications of each hodoscope plane are given in Table 3.2. A precise alignment of the hodoscopes was achieved by examining the distributions of positions of tracked muons at each hodoscope plane when a given hodoscope element in that plane was fired.

Detector	Paddle Width [cm]	Overlap [cm]	# of paddles (per half-plane)	Width × Height (per half-plane) [cm] × [cm]	z-position [cm]
H1X	7.32	0.3175	23	162 × 70	666
H1Y	7.32	0.3175	20	79 × 140	653
H2X	13.00	0.3175	16	203 × 152	1421
H2Y	13.00	0.3175	19	132 × 241	1400 (L), 1406 (R)
H3X	14.59	0.3175	16	228 × 168	1959
H4X	19.65	0.3175	16	305 × 183	2234 (T), 2251 (B)
H4Y1	23.48	0.3175	16	152 × 366	2130 (L), 2146 (R)
H4Y2	23.48	0.3175	16	152 × 366	2200 (L), 2217 (R)

Table 3.2: Parameters of all hodoscope planes. z-positions of H2Y and H4 half-planes are offset slightly due to the half-planes themselves overlapping.

3.7.2 Drift Chambers

Each of Stations 1, 2 and 3 is equipped with a drift chamber (DC) to measure the passing x and y positions of muons at its z location, with each DC flat vertical to the z axis, and a drift cell is of the box shape.. These measured positions are critical for reconstructing the trajectory of muons, and thereby their kinematics. Each DC contains six drift chamber planes, arranged in three pairs with parallel wire orientations (each pair referred to as a "view"). Wires oriented vertically (x-measuring) are referred to as being in the "X" view, and at angles of $+14°$ and $-14°$ with respect to the y-axis are the "V" and "U" planes, respectively. The second plane in each view is offset from the first by one half of a wire-to-wire distance (*"cell width"*) in order to resolve the left-right ambiguity of drift direction. This offset plane of each pair is referred to as the *primed* plane, and is denoted with a '$\prime$'. So, in each DC, there are X, X$'$, U, U$'$, V, and V$'$ planes, with primed and unprimed planes (like X and X$'$) constituting a view.

The individual drift chambers at Stations 1 and 2 are called "D1" and "D2", respectively. Station 3 has two drift chambers, since the desired acceptance area it has to cover is substantially larger than one DC can cover. These are split vertically to cover the top and bottom halves, and are called "D3p" and "D3m" where "p" and "m" stand for "plus" and "minus". Table 3.3 summarizes the parameters of the DC's. D1 and D3m have been upgraded during the data taking, as listed in Tab. 3.4. This original and upgraded versions are referred to as DN.1 and DN.2, respectively.

Chamber	Plane	Number of wires	Cell width [cm]	Width × height [cm] × [cm]	z-position [cm]
D1.1	X	160	0.64	102 × 122	617
	U, V	201	0.64	101 × 122	±20
D1.2	X	320	0.50	153 × 137	617
	U, V	384	0.50	153 × 137	±1.2
D2	X	112	2.1	233 × 264	1347
	U, V	128	2.0	233 × 264	±25
D3p	X	116	2.0	232 × 166	1931
	U, V	134	2.0	268 × 166	±6
D3m.1	X	176	1.0	179 × 168	1879
	U, V	208	1.0	171 × 163	±19
D3m.2	X	116	2.0	232 × 166	1895
	U, V	134	2.0	268 × 166	±6

Table 3.3: Parameters of all chambers. Those of primed planes are almost the same as of unprimed planes. The z-positions of U and V planes are relative to those of X planes.

Run	Period	Chamber combination
1	2012 Mar.-2012 Apr.	D1.1, D3m.1
2	2013 Nov.-2014 Aug.	D1.1, D3m.2
3	2014 Nov.-2015 May	D1.1, D3m.2
3	2015 Jun.-2015 Jul.	D1.2, D3m.2
4	2015 Sep.-	D1.2, D3m.2

Table 3.4: Combination of D1 and D3m chambers per data taking period.

The acceptance size of each chamber has been adjusted with a Drell-Yan event simulation in order to be as sensitive as possible to the x_2 range of interest. Particularly, the greater the acceptance width is, the higher the reach in x_2 is. This makes the hit-rate tolerance of the chambers a key feature, because the spectrometer is exposed to a large number of background particles, particularly near the edges where the desired x_2 events occur. It is particularly significant for the most-upstream station (i.e. Station 1) which receives the highest hit rates. Experimental data shows that the rate tolerances are 3.0 MHz/wire at D1, 1.6 MHz/wire at D2 and 0.7 MHz/wire at D3 with a beam intensity of 5×10^{12} protons/spill. The gas-amplification gain should not be degraded under these hit rates.

For Run 2 and beyond, the gas mixture used for almost all the chambers is Argon:Methane:CF4 (88%:8%:4%) with a drift velocity of about 20 μm/ns. A “fast gas” mixture used for D1.2 (upgraded D1) is Argon:CF4:Isobutane:Methylal (68%:16%:13%:3%) with a drift velocity of 50 μm/ns and thereby a better hit-rate tolerance. This is “fast” in comparison to the $\approx 20\mu$m/ns rest of the DCs. The spatial resolution of each plane is required to be 400μm, which corresponds to a momentum resolution of $\Delta p/p = 0.03 \cdot p$ (GeV/c). The resolution of dimuon invariant mass is dominated by the multiple scattering in FMAG; the chamber momentum resolution is about 10% of the total mass resolution at maximum.

The D1.1, D2 and D3m.1 chambers have been inherited from previous Drell-Yan experiments that have been conducted at Fermilab. Chambers D2 and D3m.1 have their origin in E-906 [11] and D1.1 is from SeaQuest's direct predecessor, E-866/NuSea [9, 18]. Since these chambers haven't been used for decades after the previous experiment, they had to be refurbished by restringing $\approx 30\%$ of their sense wires due to them being loose or broken. Newly supplied electronic readout boards were also mounted on these chambers.

The D3p and D3m.2 chambers were designed and constructed specifically for this experiment in order to cover the large acceptance required at Station 3. D3p was newly constructed by the TokyoTech SeaQuest collaborators and was shipped from Japan to Fermilab. The first part of data taking, Run 1, was carried out using D3m.1 while preparing for the construction of D3m.2. The newer D3m.2 is wider than D3m.1 by 25 cm at each side, allowing the high-x_2 statistics on $\bar{d}/\bar{u}$ and $Y_A/Y_{^2H}$ to increase by $\approx 20\%$ at $x_2 \sim 0.3$ and $\approx 10\%$ at $x_2 \sim 0.4$. The operational stability also improved, as D3m.1 suffered from frequent dead/noisy wires, HV trips, and leak currents. The D1.2 chamber was also designed and constructed for this experiment by the University of Colorado Boulder. As it is wider than D1.1 by 25 cm at each side and greater hit-rate tolerance, the anticipated statistics is expected in the high-x_2 region is expected to increase still more. It was installed in the experimental hall near the end of Run 3.

3.7.3 Proportional Tubes

Downstream of Station 3 and the 1 m thick iron hadron absorber wall is Station 4 with its hodoscope planes and proportional tube detectors (prop tubes). At Station 4, the only beam-induced particles that remain that can leave tracks in an ionization detector are high energy muons. The prop tubes enable the task of muon particle identification (PID) for the experiment, and consist of four planes. Each detector plane is made of 9 prop-tube modules, with each module assembled from 16 12-ft long 2" diameter prop-tubes staggered to form two sub-layers. The first and fourth planes are oriented along the horizontal direction (tubes parallel to the floor) to provide positional measurements in y, as shown in Fig. 3.9. The second and third planes are arranged vertiacally to measure x-position as shown in and Fig. 3.10.

Each plane of proportional tubes is composed of 9 *modules*, which each have a set of 16 proportional tubes: 8 in lined in an horizontal or vertical orientation and 8 more offset ("primed") from the first 8 by 0.5 inches. This offset structure prevents any muons from going undetected between tubes and allows for left-right disambiguation for two hits in adjacent primed-unprimed sub-plane pairs in the same module. The

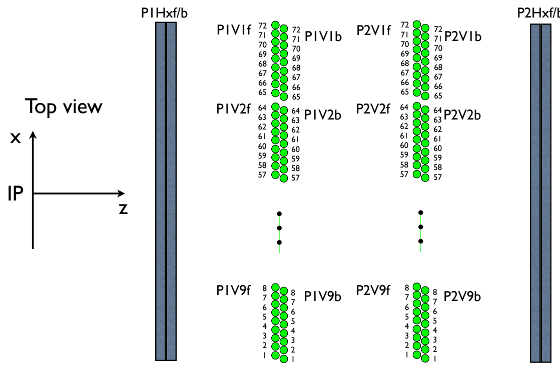

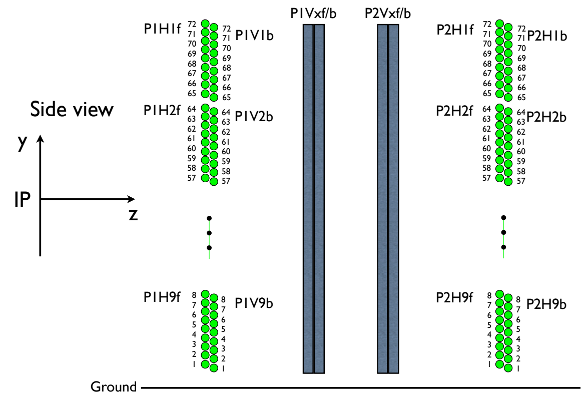

Figure 3.9: Proportional tube top ($x-z$ plane) view. Figure 3.10: Proportional tube side ($y-z$ plane) view.

modules are labeled $1-9$ in increasing order from left to right for the $x-$measuring planes and from $1-9$ in increasing order from top to bottom. So, the top module of the first vertical plane of prop tubes is P2H1. Additionally, in each module, the primed and unprimed sub-planes are referred to as f for "front" (facing upstream) and b for "back" (facing downstream). This substructure can be seen in detail on Fig. 3.9 and Fig. 3.10.

A single prop tube is made of 2-inch diameter aluminum tubes with wall thickness of 1/16 inches. The central anode wire is a gold-plated 20μm diameter tungsten wire kept at approximately 1.95 kV. Considering the staggered nature of each plane's substructure, one can in principle achieve a spatial resolution of 0.3mm. During Runs 2 and 3 of data taking, a resolution of 0.5mm for high energy muons was observed, which is more than sufficient for muon identification purpose. The gas mixture for prop-tubes is P-10 (Ar:Methane = 90:10) mixed with a 10% CF4 gas (Ar:CO_2:CF_4 = 70:20:10) which yields the maximum drift time about 400ns. With this maximum, the prop tubes can handle a singles rate up to 2MHz, while normal operational hit rates are typically below 1MHz.

A typical desired high-energy muon within spectrometer acceptance will traverse through two prop-tubes in each plane and induces hit signals on two anode wires. The path of track is reconstructed from the drift time measured on the two anode output, with a custom TDC board that provides 0.44 ns timing resolution. With the hit information reconstructed from readouts of the forward and backward planes in $x-z$ and $y-z$ direction, precise reconstruction of the track trajectories can be obtained. Ideally, 8 hits from the 4 planes are used to form a track pointing back to the target. If such is the case, a candidate muon track is successfully identified.

Detector Plane	Number of modules	# tubes per module	Width (x) × height (y) [cm] × [cm]	z-position of front (back) sub-plane [cm]
P1H	9	16	368 × 368	2,099 (+4)
P1V	9	16	368 × 368	2,175 (+4)
P2V	9	16	368 × 368	2,367 (+4)
P2H	9	16	368 × 368	2,389 (+4)

Table 3.5: Parameters of the four proportional tube planes.

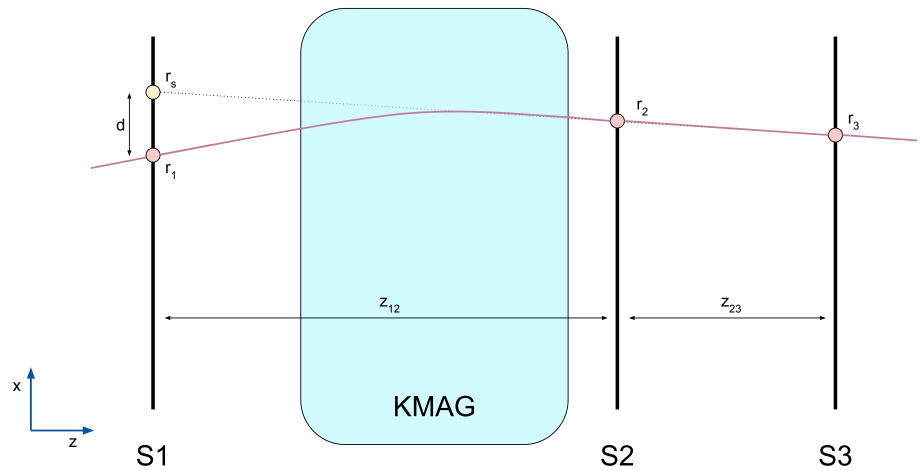

Figure 3.11: A simplistic depiction of a track passing through from Station 1, through KMAG where its path is bent by the magnetic field, and then straight on through Stations 2 and 3.

3.7.4 Mass Resolution from Chamber Resolutions

The mass resolution of the spectrometer is, in part, limited by the resolution of the tracking chambers and the distances between them. For an arbitrary set of hit positions in Stations 1, 2, and 3 (r_1, r_2, r_3) which are separated from each other in z by distances z_{12} and z_{23}, with KMAG in between Stations 1 and 2 supplying a P_{kick}, one can derive $\Delta P/P$. A line, or track segment, is first reconstructed between r_2 and r_3. The slope (and its uncertainty) of this track segment in the $z-x$ plane is:

$$s_{23} = \frac{r_3 - r_2}{z_{23}} \quad , \quad \Delta s_{23} = \frac{1}{z_{23}}\sqrt{\Delta r_3^2 + \Delta r_2^2} \tag{3.3}$$

The values of Δr_n here are the position resolutions of the individual tracking chambers at each Station. One can use this slope to project a trajectory through KMAG and onto Station 1. The momentum is calculated by seeing where the actual hit position is in Station 1 and looking to the distance (d) between where the particle hit the station and where it would have hit had KMAG's magnetic field not existed. This is called a *sagitta analysis*, as the magnetic field moves the particle's trajectory as if along a circle, and we are looking to the particle's path along the sagitta of that circle. Ultimately, the momentum uncertainty is related to this distance as:

$$\frac{\Delta P}{P} = \frac{P}{P_{kick}}\Delta d \tag{3.4}$$

The expected sagitta point (r_s) is located at:

$$\begin{aligned} r_s &= s_{23}z_{12} + r_2 && (3.5)\\ \Delta r_s = \sqrt{\Delta s_{23}^2 z_{12}^2 + \Delta r_2^2} &= \sqrt{\Delta r_3^2\left(\frac{z_{12}}{z_{23}}\right)^2 + (1 + \left(\frac{z_{12}}{z_{23}}\right)^2)\Delta r_2^2} && (3.6)\end{aligned}$$

And the distance, d follows as:

$$\begin{aligned} d &= r_s - r_1 && (3.7)\\ \Delta d = \sqrt{\Delta r_s^2 + \Delta r_1^2} &= \sqrt{\Delta r_3^2\left(\frac{z_{12}}{z_{23}}\right)^2 + (1 + \left(\frac{z_{12}}{z_{23}}\right)^2)\Delta r_2^2 + \Delta r_1^2} && (3.8)\end{aligned}$$

The momentum resolution due to chamber resolution can therefore be described as:

$$\frac{\Delta P}{P} = \frac{P}{P_{kick}}\sqrt{\Delta r_3^2\left(\frac{z_{12}}{z_{23}}\right)^2 + \left(1 + \left(\frac{z_{12}}{z_{23}}\right)^2\right)\Delta r_2^2 + \Delta r_1^2} \tag{3.9}$$

The dependence of the resolution on P/P_{kick} works such that the larger the P_{kick} is (w.r.t. particle momentum P), the more the track is bent, and the more precisely the original momentum is defined. Besides chamber resolution, other contributions to this momentum resolution are from multiple scattering through FMAG's iron beam dump and from the spectrometer's angular resolution. These will be discussed elsewhere in this paper.

The mass resolution is linked to momentum resolution via the following relation

$$\frac{\Delta M}{M} = \frac{\Delta P}{2P} \tag{3.10}$$

The factor of two arises from the fact that the Drell-Yan dilepton mass comes from two independent muons with the same momentum resolution. This mass resolution is important because it, in turn, contributes to the $\Delta x_2/x_2$ resolution, which is the key dependent variable for SeaQuest measurements.

$$\frac{\Delta x_2}{x_2} \approx 0.57\Delta x_F + 0.012M^2\frac{\Delta M}{M} \tag{3.11}$$

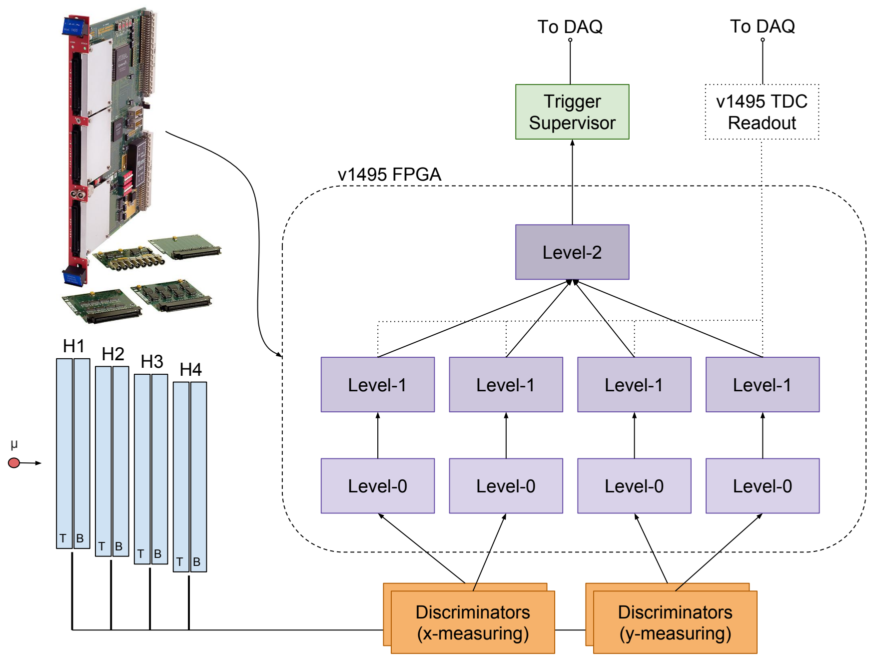

Figure 3.12: The trigger system at SeaQuest is composed of 9 CAEN v1495 FPGA modules. These modules output a trigger signal to the Trigger Supervisor, which tells the DAQ when to record data.

3.8 Trigger

The SeaQuest Trigger System is designed to quickly select candidate dimuon events from the high-rate, high-background environment using discriminated hodoscope signals.

3.8.1 Design Requirements

The trigger must select events of interest to the main physics goals with good enough efficiency (maximum signal-to-background ratio) to facilitate high-statistics analyses. In general, it is optimized to accept high-mass ($4-10$GeV) dimuons originating from the targets and beam dump. The event selection is also designed to intentionally reduce acceptance of dimuons from other, higher-rate sources, such as J/Ψ decays and non Drell-Yan dimuons originating from the beam-dump, though enough J/Ψ events are triggered on to allow high-statistics analysis of J/Ψ physics. Other goals of the trigger design is to keep the triggering rate low enough to maintain an acceptable DAQ livetime and to keep the trigger's internal throughput deadtime-free. By design, there should be no bottleneck at this stage, and the trigger should be capable of firing on any and all RF-buckets while the DAQ is live.

The hardware, firmware, and design should be sufficiently flexible to quickly accommodate changes in the spectrometer, beam conditions, and physics goals. Any changes to the geometric acceptance of the spectrometer, such as new/moved detectors or changes in the magnetic fields must be immediately reflected in the trigger selection in order to maintain high-signal efficiency and good background rejection power. Similarly, a change in the beam duty factor or intensity should be accompanied by a change in the event selection, ensuring trigger rate optimization and zero internal deadtime. Finally, the trigger should be capable of specific modifications to facilitate special runs for other physics goals. For these reasons, the design of the trigger system underscores a significant need for flexibility in its hardware and design.

Lastly, the design of the trigger system should include self-diagnostic capabilities, allowing for constant monitoring of the trigger system's performance. Internal pulser-testing is employed to test the function of each compiled firmware every time the trigger logic changes. For added transparency, data from the internal TDC's is used by online and offline software to monitor the self-consistency of the trigger for each recorded physics event.

3.8.2 Trigger Hardware

The triggering system, which is depicted in Fig. 3.12, begins with the Stations 1-4 hodoscope arrays. Hodoscopes are used for this task as the time resolution and high speed is limited only by the speed of light through the scintillator paddles and secondary emission of electrons (through the stages of the PMTs. This occurs over the span of nanoseconds, which allows for fast triggering on RF buckets that occur every 19ns during spills. The hodoscope planes - both x- and y-measuring planes - are separated into top and bottom sections as far as triggering is concerned. The signals from the hodoscope arrays are passed through a set of discriminator modules, which will only pass a signal on to the rest of the trigger if there is enough of a signal from the PMT's past a preset threshold.

The output of the discriminators is passed along to one of the nine CAEN v1495 FPGA (Field Programmable Gate Arrays) VMEbus (Versa Module Europa) modules [3]. This hardware trigger consists of a single decision stage with a three-step parallel pipeline. These steps are referred to as the *level-0*, *level-1*, and *level-2* stage triggers. The detailed internal flowchart of the CAEN v1495 electronics can be seen in Fig. 3.13.

At the first step, level-0, there is nothing actively performed during nominal data taking. The signal is passed on through, unaltered, to level-1. As it stands, level-0 is not used for any of the triggering modes. This stage is, however, extensively used for the pulser testing and self-diagnostic purposes. The level-0 stage is capable of being programmed to pulse arbitrary patterns on to the level-1 stage, which is very useful for observing how level-1 (and subsequently, level-2) will behave in a controlled setting. Whenever a new firmware is installed on the v1495, a pulser test is performed to ensure that all design requirements are met

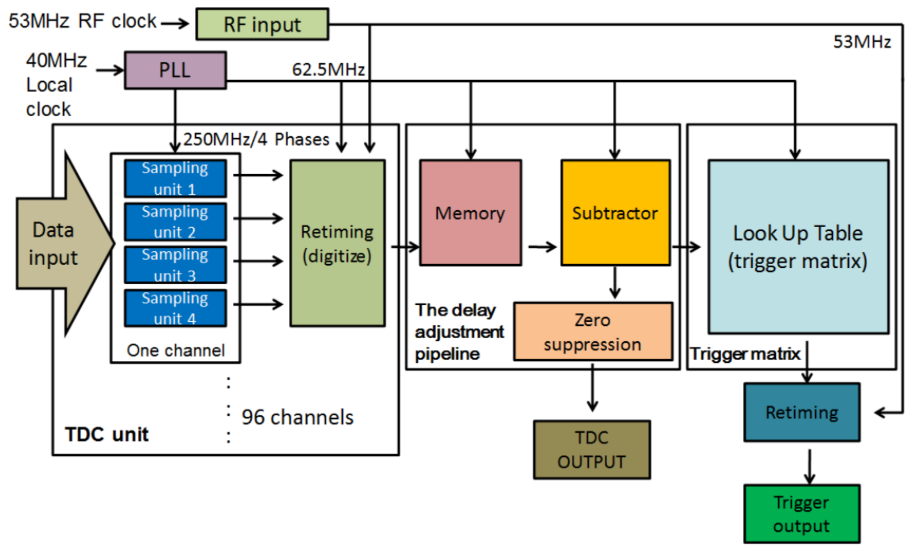

Figure 3.13: A block diagram of the major functions of the v1495 FPGA [17].

before uploading the firmware for production data taking.

The next level-1 trigger records the hit signals from the x- and y-measuring hodoscope hits, split into top and bottom partitions with respect to their location in the SeaQuest spectrometer. The hit patterns are tested via a lookup table against a preselected set of hodoscope hit patterns, or *"trigger roads"*. Each trigger road corresponds to a set of four hodoscopes: one from each station, with all being in the top or bottom half of the spectrometer. In this lookup table, there is a charge and approximate p_T value for each preselected road. These are known via studies of Monte Carlo studies of muon paths from di- or single-muon events originating from the targets or beam dump. The roads were selected such that as many good dimuons are selected while reducing roads that are dominated by background signal that might cause trigger and/or DAQ deadtime.

During data taking, only the x-measuring hodoscopes were used for the v1495 trigger. As such, the two level-1 stages that look to the y-measuring hodoscope signals were unused. The level-1 trigger logic identifies four-out-of-four X1-X2-X3-X4 coincidences, which are characteristic of high p_T single muons produced from the targets or beam dump. Each time a candidate coincidence that satisfies a preselected road is found, the level-1 step outputs certain logical bits indicating the track's charge, detector half (top or bottom), and p_T bin.

The third step of the triggering logic is the level-2 trigger, or the *"Track Correlator"* stage. This step takes the outputs of level-1 (charge, detector half, p_T bin) and finds if any combinations satisfy any of the preprogrammed triggering modes. If one of these modes was satisfied, a signal is sent to the Trigger Supervisor (TS) module that communicates with the DAQ system to record an event at a specific synchronized

RF bucket.

3.8.3 Triggering Modes

The v1495 FPGA had five configurable sets of physics triggers were used in the trigger system for the majority of production-level data taking. These five are referred to interchangeably as "Matrix" and "FPGA" triggers, followed by the number 1-5 indicating which of the five. These modes are described in detail in Table 3.6.

Trigger	Condition	Sign	$\#\mu$	Prescale
FPGA-1	$T \wedge B$	Opposite	2	1
FPGA-2	$(T \wedge T) \vee (B \wedge B)$	Opposite	2	1000
FPGA-3	$T \wedge B$	Same	2	123
FPGA-4	$T \vee B$, all p_T	$+ \vee -$	1	30000
FPGA-5	$T \vee B$, $p_T > 3GeV$	$+ \vee -$	1	2000
NIM-1	Y-coincidence	NA	NA	30000
NIM-2	X-coincidence	NA	NA	1000
NIM-3	Random RF	NA	NA	1000

Table 3.6: Trigger settings for Run 3 and beyond. Prescale figures shown are typical values, and were adjusted as experimental needs were tuned. NIM-1 and NIM-2 triggers' exact conditions could be changed and reconfigured from the counting room.

Different trigger settings were used for capturing data for different purposes. The primary triggering mode is FPGA-1, which looked for a combination of two roads of opposite sign that reside in opposite halves of the spectrometer. The FPGA-2 looked for good muon pairs that occurred in the same half. This, however, turned out to have a combinatoric problem that had two adverse effects: track reconstruction was difficult for these types of events, and the trigger fired off too often, causing high trigger and DAQ deadtime. As such, FPGA-2 was disabled for much of data taking. FPGA-3 trigger looked for the same kind of signal as FPGA-1, but with same-sign muon pairs. This type of event is useful for analyzing the experiment's combinatoric background. FPGA-4 and -5 are "singles" triggers that record events that are useful for estimating backgrounds and detector efficiencies. Each of these has a *"prescale factor"* that limits how many of each mode actually fires the trigger. For example, FPGA-3 has a prescale factor of 123, which means that, within a single spill, there has to be 123 FPGA-3 events before it tells the DAQ to record one. This keeps certain high-frequency trigger modes from dominating the readout and causing undue deadtimes.

In addition to the v1495 FPGA triggering mechanism, the outputs of the hodoscope discriminators are also sent up to the control room to a set of NIM logic modules. These signals, however, do not describe each hodoscope paddle, but are *AND*s of the tops and bottoms of each plane. For example, if one or more paddles in H1T fires, then a positive signal is sent out indicating that H1T fired. These signals can be used to form a rudimentary trigger on situations such as 4- or 3-out-of-4 coincidences in the X- or Y-direction hodoscope planes. In general, NIM-1 is used for Y-coincidences, and NIM-2 is used for X-coincidences.

The third NIM trigger mode is of particular importance, as it is used for estimating a great deal regarding backgrounds and rate dependence issues. The NIM-3 trigger is called the "Random RF" trigger, as it is controlled by two different clocks beating against each other. When the two clocks are in coincidence, they will send a signal to the Trigger Supervisor to record the event corresponding to the next immediate RF bucket. This trigger allows the experiment to get a random sample of the events that are occurring at the spectrometer, notably without a bias that a selective trigger can incur.

3.9 Data Acquisition Systems

The whole of the SeaQuest experiment spans two sectors of the NM beamline (NM3 and NM4) and records not only detector data, but also accelerator and atmospheric conditions. Designing a data acquisition (DAQ) for this experiment therefore requires a bandwidth and timing which cannot be provided by a single central computer system. SeaQuest has therefore employed four separate DAQ subsystems called "Main DAQ", "Scaler DAQ", "Beam DAQ" and "Slow Control". Main DAQ records the main detector information and the trigger timing. Scaler DAQ records various scaler readouts once per spill to reduce bias from the dead time of Main DAQ. Beam DAQ records information from a beamline Čerenkov detector read out by its QIE board. The Slow Control is a catch-all for everything else, from magnet current to radiation monitors that is read out once per spill.

3.9.1 Main DAQ

The MainDAQ is powered by a Jefferson Lab developed software package named CODA (CEBAF[1] On-line Data Acquisition). The Trigger Supervisor could receive up to 12 different kinds of triggers. The first four triggers (FPGA 1-4) can be prescaled up to 24 bits. The second four triggers (FPGA 5, NIM 1-3) can be prescaled up to 16 bits. The rest of triggers (NIM4, flush trigger, Beginning of Spill (BOS), End of Spill (EOS)) are not prescalable. The Main DAQ can configure which triggers are enabled at the Trigger Supervisor level and what the prescale factors are for each triggering mode. Once the TS receives a trigger, it will count the prescale factor and, based on how many triggers of that type have fired so far, it will decide if the Main DAQ will accepted trigger or not.

Once the TS accepts the trigger, it send an "accepted trigger" signal to the other front end electronics, such as the detectors' TDC readouts. Facilitating intercommunications, the Main DAQ system is connected

[1]The old acronym inside of an acronym bit. CEBAF: Continuous Electron Beam Accelerator Facility

to the TS and the CPU's in the VME crates via a local network. These CPU's are known colloquially at SeaQuest as readout controllers, or ROC's. The TS connects with each VME crate, and when the TS sends an "accepted trigger", an interrupt signal is sent to each of the ROC's. The ROC's will then start reading the various front-end electronics (FEE).

The TS also sends a signal to the to QIE of the BIM, and the QIE retains information regarding the ± 16 RF buckets around that triggered RF bucket to assist in investigating the beam quality around each of our event triggers. The output of the QIE is encoded into a scaler latch card format. If the beam intensity in RF buckets neighboring the trigger is higher than the user-select threshold, then the board will issue a veto signal to the TS to ignore this trigger.

The Main DAQ's deadtime is considerable, as it has to communicate with the TDC's, which have the longest copy-in-progress time of $32\,\mu$s. The average TDC readout time is approximately 300 ns per 32bits (one hit), and as such, the slowest ROC which contains 7 TDCs has, on average, $150\,\mu$s deadtime. This deadtime is accounted for under the umbrella term of *"busy"* time and factored into the calculation of the "live protons" received by the experiment.

3.9.2 Scaler DAQ

The Scaler DAQ is used to ensure that the detector and trigger systems are working properly. The read out controller CPU is a MVME5500 [12] with four scalers. One the these scalers is triggered by the coincidence of a 7.5 kHz gate generator and the beam spill signal. This records the 7.5 kHz response of the hodoscope arrays. The other three scalers are triggered by the BOS or EOS signals and thus record spill-level rates. Data collected by these spill-level scalers are the number of times each Main DAQ trigger is satisfied (both raw and accepted), intensity of the beam, and the rates of the hodoscope arrays. The readout of this VMEbus DAQ is done using CODA very similarly to the Main DAQ, but on a completely different system. An independent program analyzes the data in real time in order to monitor the performance of the detectors and triggers, as well as the quality of the beam.

3.9.3 Beam DAQ

The Beam DAQ is composed of a Čerenkov detector in the proton beam (the Beam Intensity Monitor discussed earlier in this chapter), a QIE board, and a custom C++ program to control their operation and read out. The Beam DAQ is responsible for recording the 53 MHz structure of the beam, i.e. the intensity of each RF bucket. Its calculation of the 53 MHz duty factor $DF = \frac{<I>^2}{<I^2>}$ is the primary measure of beam quality that accelerator operators use for tuning. In short, the duty factor is a measure of the *uniformity* of

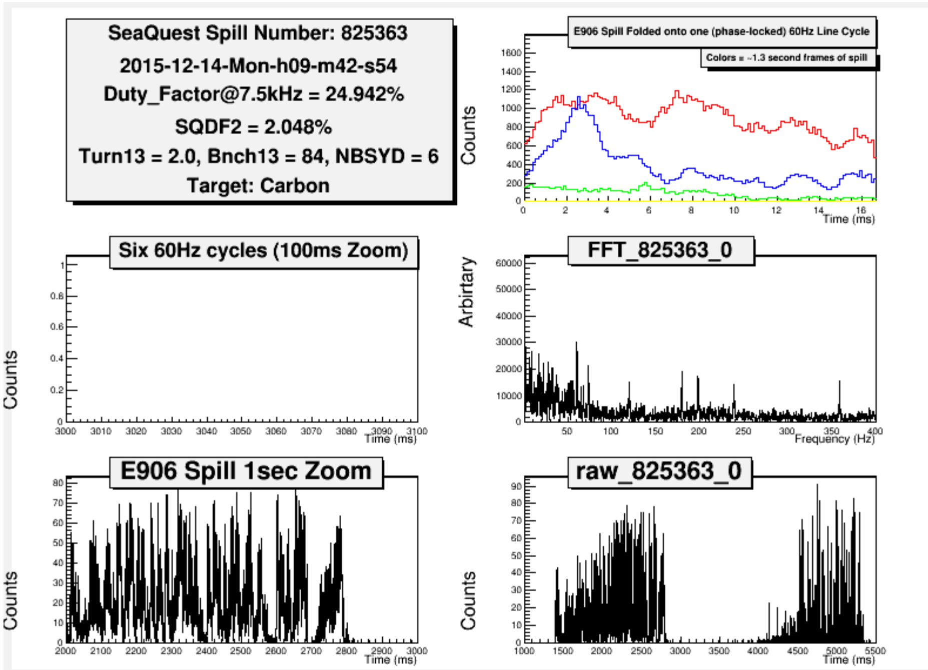

Figure 3.14: A standard Beam DAQ display showing beam characteristics and spill data. The bottom two plots show the output of the QIE on a ms scale.

the intensity of the beam. If we were to ignore the buckets intentionally left empty, and if it were to be the case that every RF bucket had the same number of protons, the 53 MHz duty factor would be 100%.

There four types of data recorded by the QIE have already been covered in the Beam Intensity Monitor section: QIESum, beam inhibit, busy time, and the ± 16 RF bucket intensities. The Beam DAQ commences read out of each of these blocks of data when the EOS signal is seen. The block of QIE data for all buckets is about 300 MB. To read this much data in time to analyze it and be ready for the next spill, the DAQ program utilizes multithreaded processes. Three threads are used to read the data from the QIE board's three ethernet chips, and up to eight threads are used to analyze the data. Analyzed data is displayed on a public webpage so that shifters and accelerator operators can monitor the quality of the beam (Fig. 3.14). The fully processed data is also written out to tab-delimited ASCII files, which are archived and also uploaded to our online MySQL server.

3.9.4 Slow Control Readout

The Slow Control readout system is an aggregation of many different readouts from various parts of the experiment. This is also the umbrella term for other critical monitoring and book keeping tasks that must be performed. The one common thread to them all is that they only *need* to be read out / performed once per spill in order to give perspective on the conditions of the experiment for each given spill. The term

"Slow" in Slow Control is adapted from the term "Slow Spill", which is used to characterize the method of beam delivery to SeaQuest. The Slow Control is run by an array of Python, Perl, and Bash scripts that, for the most part, run independently. These scripts primarily interact with and read out from EPICS, ACNET, and the local Spill Counter.

EPICS, ACNET, and Kiethley

The EPICS software package (Experimental Physics and Industrial Control System) is used for communicating any number of variables across the experiment's local network. EPICS is used for feeding readouts from many different sources and formats, and making them available to any other system that may have need of certain information, but does not natively communicate with a different system's format. Bridging this gap, EPICS is able to gather information regarding the target, beam, and environmental data into one place.

The EPICS server is installed on SeaQuest's target control computer, where the target position, pressures, temperatures, and proximity sensors are monitored and controlled. These values are critical to track and monitor, as they affect what target is in position at any given spill, along with information that may infer the cryogenic liquid targets' densities. Additionally, there is information regarding the operational mode of the target table, such as whether or not the target table is being manually controlled or if it is automatically repositioning itself. In Slow Control parlance, information from the target computer that is sent to the EPICS server is labeled as "Target" type data.

Several values are read into the EPICS server from the Accelerator Network (ACNET), which monitors many critical systems. Beam intensities (S:G2SEM) and FMAG / KMAG currents are two of the major factors that must be factored in for any analysis. There are additional readouts with esoteric names that can record anything from beam pipe vacuum to upstream radiation monitors. It is important to note that the FMAG and KMAG variables from ACNET are read out to the EPICS server every 3 s, particularly because it is unsafe to deliver beam to the sensitive detectors without FMAG being fully powered. As such, the FMAG current is read into the beam interlock system. In the Slow Control feed, this type of information is labeled as "Beam" data.

Finally, there is a Keithley multimeter [*citation needed*] in SeaQuest Hall near the electronics racks by Station 3. This device has the responsibility of relaying information regarding ambient temperature, air pressure, and humidity up to the control room. This information on its own is not typically used for any analyses, but in the case that, for example, a rise in humidity results in any electrical device failures, the monitoring data exists to diagnose it as such. This data is gathered by a 'kscan' program that is run on the target machine, and its operation typically takes 11s to return a result. Data from the Keithley multimeter that is put into the Slow Control feed is labeled as "Environment" data.

Spill Counter

Perhaps one of the most critical components of the data acquisition is the coordination between the many sources of data in the DAQ. The Main DAQ, Scaler DAQ, Beam DAQ, and Slow Control do not share a single clock or network, so some measures need to be taken to ensure that data from different sources regarding a single spill's worth of data actually all correspond to the same spill. The concept of a locally maintained Spill Counter arose as a solution to this problem, and it is handled in the form of a simple Python script and a flat text file containing a single integer.

The enacted solution begins with placing an initialized spill counter (*spillID*)value (currently $O(10^5)$) into an otherwise empty text file at a specified location. Then, when the ACNET readout receives a BOS/EOS signal from AD, a simple python script performs the following:

- Read the current spillID from the file
- Broadcast this value over the EPICS server
- Insert a single ASCII-encoded event into the Main DAQ and Scaler DAQ CODA streams containing only that spillID number
- Waits for 20s while other scripts may want to use the current spillID value to connect its value to the spill that just ended
- Updates the file to contain spillID + 1

This simple approach has been very effective in its usage so far, and the spillID incremented via this method has been shown to be accurate upon scrutiny of data contents across DAQs. This can be easily done by looking at a series of full and empty spills, as it is obvious which spills had beam and which did not investigating the output of each DAQ. The weakness lies in the fact that this system relies on a single file, which is susceptible to any number of file access and timing issues. At some point in the future, it would be advisable to have all spillID-using systems to read the current value from the broadcasted EPICS server value instead of having several applications attempting to access and read the single file (even if just read-only).

Python Slow Control Script

With all of this going on to aggregate data from several sources, there is one final script that takes this aggregated data and makes it readily available for the rest of the DAQ systems. A `read_slowcontrol.py` script, once every 60 s supercycle, puts the following together into a single ASCII text file:

- Clock time ("vxticks") of the Trigger Supervisor
- Spill count data
- Beam data
- Environmental data
- Target data
- Timestamp

Once all of this is written to a file, this is sent to the Main DAQ and Scaler DAQ to be integrated into the full CODA file as a plain text event with a simple, tab-delimited format.

Chapter 4

PMT Upgrade

During Run I of SeaQuest, observations of hodoscope wire maps (as in Fig. 4.1) suggested an apparent drop in expected performance in the $y-$measuring hodoscopes. While this performance was most obviously seen in the $y-$measuring hodoscope planes, the $x-$measuring planes were likely also affected. This effect was assumed to be due to high-intensity RF buckets that caused very high multiplicity in all of the detectors in the spectrometer for that event. The result of these intense events seemed to push the PMTs and/or their PMT base electronics past their operational capacity.

The understood cause of this *"sag"* in performance, as it came to be called, was due to a destabilization in the voltage divider in the PMT base. This critical component holds each dynode stage at a specific voltage, and when this destabilizes and is unable to maintain an appropriate voltage difference between dynode stages, inefficient performance of the PMT results.

During the Fall of 2012, prototyping and testing was performed with the goal in mind being to assemble a new base for the Philips XP-2008 PMTs [14] and compare its performance to the original PMT base and to some modern, high-performance Hamamatsu PMTs. Once a base design tested well, the new bases would be manufactured and installed in the existing frames of the original PMT bases.

4.1 PMT Basic Construction and Operation

Figure 4.2 shows a schematic design of a typical photomultiplier tube and base setup. It consists of a photocathode that is followed by an electron multiplier section (or dynode string) then an anode from which a final signal is delivered. During operation, a high voltage is applied to the photocathode, dynodes, and anode in such a way that there's a potential "ladder" going from stage to stage. When an incident photon from the hodoscope scintillator paddle hits the photocathode, an electron is emitted via the photoelectric effect. The voltage difference between the cathode and dynode stages draws the emitted electron to the dynodes, and each time an electron hits a dynode, some of that electron's energy is transferred to other electrons in the dynode. These electrons then are emitted and become accelerated towards the next dynode

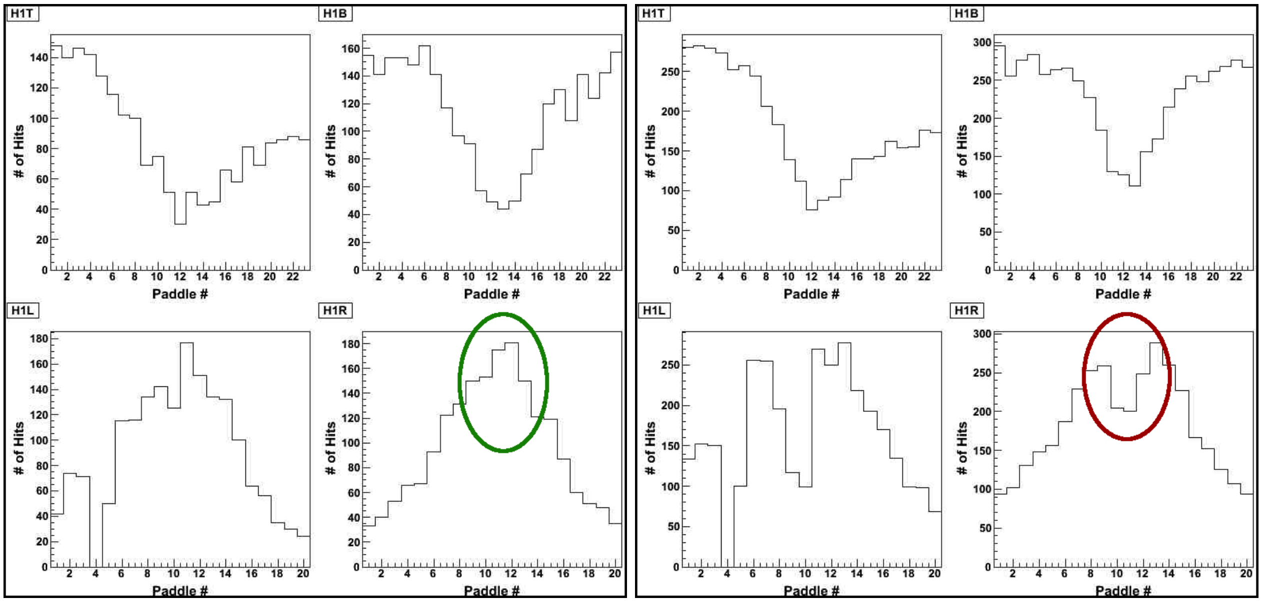

Figure 4.1: (Left) Histogram of hodoscope ‘hits’ in a typical event; (Right) Histogram of high-intensity event, with marked sagging most noticeably in the middle of the y-measuring hodoscopes

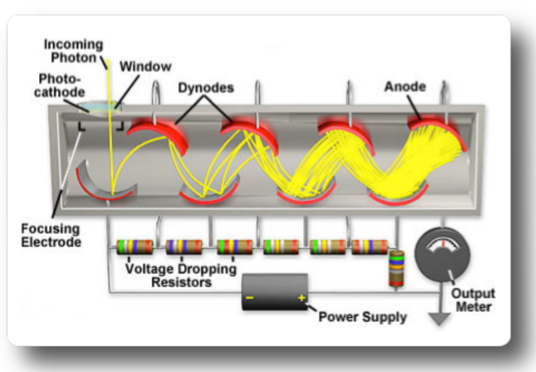

Figure 4.2: A diagram of typical PMT operation. The circuit controlling the voltage-dropping resistors is the part that was upgraded in this chapter.

stage. This process is called secondary emission, and by the time the process is repeated, there is a cascade or avalanche of electrons that land on the anode, resulting in a signal that can be amplified and analyzed.

It is the case that the voltage divider ultimately supplies the electrons that are emitted in this signal cascade. If too many photons and resultant electron cascades occur, the dynode stages' voltage divider will destabilize as they attempt to resupply the the dynode stages with electrons. The problem that was experienced at SeaQuest was that these high-intensity events were flooding the PMTs with photons, causing this "saturation" which caused this destabilization and the inefficient performance that was observed. The goal specifically was to test out modern base designs that provided for added stability to the performance of the voltage divider, even under high rates.

In general, each base divides around a -1500 V potential total over the photocathode (K), ten dynode stages (D1-D10), and the anode (A). There are two currents that are referred to here:

- Signal Current: This is the signal that passes over the anode, which is the end-result of the cascading secondary emission electrons from each dynode stage.
- Bleeder Current: This is the current through the voltage divider. It is termed the "bleeder" current since the compounding electrons in the signal current must be "bled" from the current through the voltage divider.

Throughout these voltage base designs, capacitors are commonly implemented in the latter dynode stages where the most electrons are emitted. These capacitors, when charged, are able to replenish the lost charge on its corresponding dynode stage in the event that an intense light pulse induces a large signal current. As the capacitor is able to hold its own charge, this resupply can occur without requiring the charges to be drawn from the bleeder current, thereby keeping the voltage across the dynode stages more stable.

4.2 PMT Base Design Iterations

There were several iterations of base design to determine which was best to approach for full base production and installation at SeaQuest. The core addition was the inclusion of transistors between dynode stages, according to the improvements suggested by C.R. Kerns in his paper regarding high-rate PMT bases [10]. Common solutions to destabilization in PMT bases have been to have (1) very large capacitor banks with charges $> 10^3$ times greater than the time-averaged dynode current and/or (2) miniature on-board,separately-powered Cockroft-Walton power supplies for the final dynode stages. A Kerns-style transistorized base allows for a light-weight, small size, and simple base that does not require extra power supplies or voluminous energy storage capacitors.

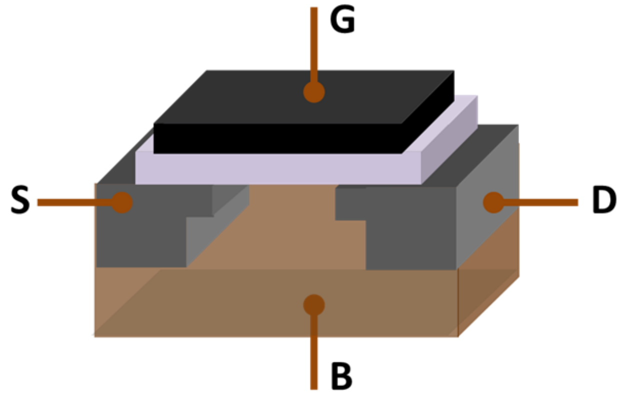

Figure 4.3: MOSFET showing gate (G), body (B), source (S) and drain (D) terminals. The gate is separated from the body by an insulating layer (white) [13]

In general, there are three important features that were tuned in this set of prototypes that affected the performance of the phototubes:

- Lower resistance
- Transistors (with protective diodes)
- Distribution of voltage division

Lower overall resistance of the voltage divider increases the bleeder current. This means that the base will be more capable of handing high-intensity, as it will be better able to replenish the charges on each dynode stage in the case of a large signal. Typically, the larger the bleeder current, the larger the signal current can be without destabilizing the voltage divider. Higher rates usually put higher demand on the signal current, so by reducing the overall resistance, one can easily increase the rate capability. The shortfall here is that with voltage constant and resistance decreased, according to Ohm's Law ($V = IR$), the current will increase. As a result, the power dissipated by the circuit ($P = I^2R$) will go as I^2, and the PMT base may heat up to critical temperatures faster than it can dissipate the heat as there is no significant ventilation in the PMT base enclosure. The Philips XP-2008 manual quotes that for continuous usage and storage the ambient temperature should not exceed $50°C$ ($122°F$). In addition to heat concerns, there's typically a power rating for the class of small on-board resistors that were planned to be used. Approaching or exceeding that power limit would run the risk of burning out a resistor and rendering the base inoperable.

Metaloxidesemiconductor field-effect transistors (MOSFETs) are introduced here to maintain the proper voltage division. In general, MOSFET transistors have an *source*, a *drain*, and a *gate*, where current flows freely through from the source to the drain, gate permitting. If at any point a certain voltage across the

Recommended voltage divider

Type A for maximum gain

K		D1		D2		D3		D4		D5		D6		D7		D8		D9		D10		A	
	2		1		1		1		1		1		1		1		1		1		1		(total :12)

Type B for bets timing / linearity compromise

K		D1		D2		D3		D4		D5		D6		D7		D8		D9		D10		A	
	2		1		1		1		1.25		1.25		1.5		2.25		2.25		2.5		2.25		(total :18.25)

K: photocathode Dn: dynode A: anode

Figure 4.4: Suggested voltage division schemes for gain vs. timing/linearity compromise [14].

gate of the transistor is not supplied (here, the voltage across dynode stages), then the source-to-drain current through the transistor is stopped until the proper gate voltage is restored. This helps greatly to “intelligently” regulate the voltage across the dynodes. Wherever transistors are used, diodes are also implemented to prevent the unlikely case of a current moving across the transistors in the wrong direction. This protects the transistors from being damaged particularly when powering the circuit on and off.

Finally, the specific division of voltage across each stage, from D1 to A, has an influence on the behavior of the PMT operation. As we see from the operations manual of the phototube in Fig. 4.4, in the case of a progressively increasing voltage division, there is a good compromise between timing and linearity. With respect to phototube operation, “linearity” is the quality that the amount of charge deposited on the anode is linearly proportional to the energy of the incident photon. “Timing”, on the other hand, is the quality that the time it takes for a high-energy photon signal and a low-energy photon signal to progress through the stages should be the same. For the purpose of optimization at SeaQuest, we wish to optimize the amount of signal (i.e. amplification or *gain*) that the phototube can accommodate. For this, the recommended voltage partitioning is flat from D1-A [14].

4.2.1 Original Base

The base that came attached to the PMTs were manufactured specifically for use by the ARGUS experiment, which was a relatively (by SeaQuest standards) lower-rate collider experiment that used e^+e^- annihilation at the *DORIS II* ring at DESY. After their tenure at ARGUS, they were handed down to the HERMES experiment located at the *HERA* polarized electron accelerator at DESY.

Though no actual circuit diagram was documented for the original PMT base, it was dissected and each component was measured. The results can be found in Fig. **??**, and its voltage division seen in Fig. 4.6. It features a simple string of resistors with capacitors of increasing capacitance along the last six stages. The voltage division can be recognized to be similar to the timing-linearity compromise scheme described in Fig. 4.4. The hope is that introducing MOSFET transistors, tuning the resistance, and altering the voltage

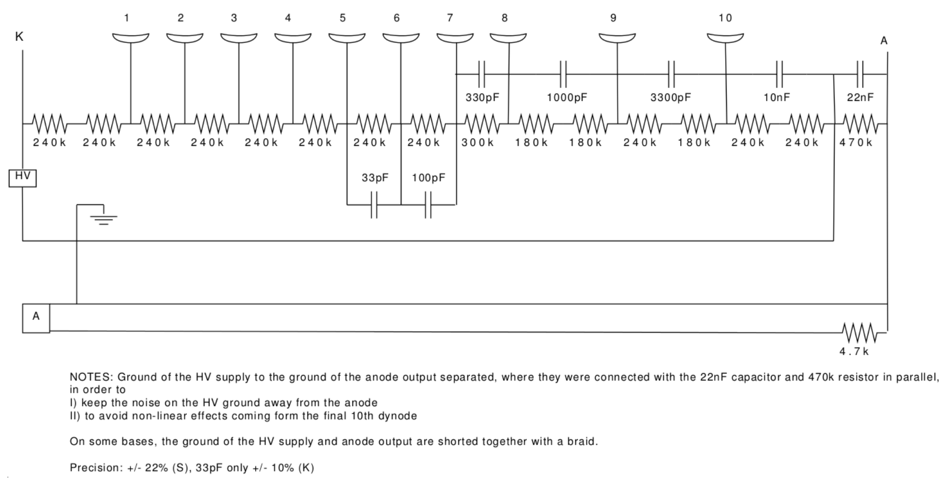

Figure 4.5: The original PMT base inherited from the ARGUS and HERMES experiments.

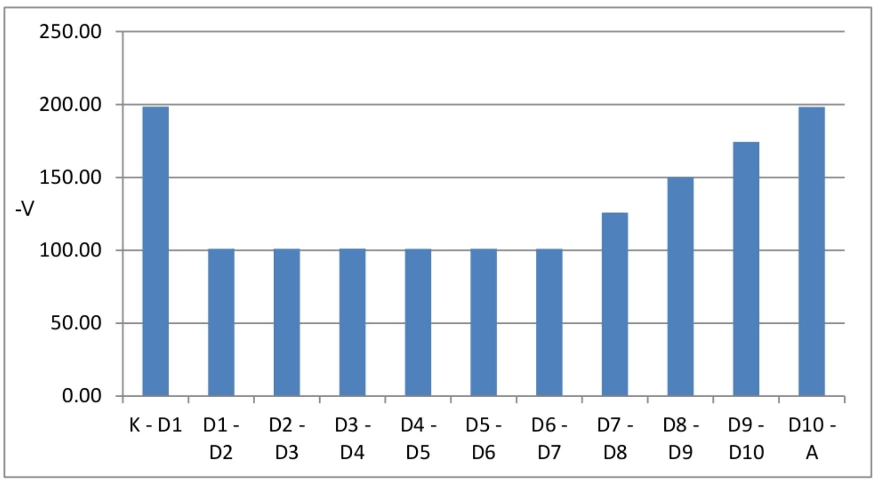

Figure 4.6: The voltage division between subsequent stages for the original PMT base design.

division will yield better high-rate performance.

4.2.2 Prototype Base v1

Once the task was set to update the PMT base design, the Fermilab Particle Physics Division was consulted on the matter. In 2010 a base design with similar goals for the exact same PMT model was designed by Sten Hansen [8]. The circuit diagram for the new base can be found in Fig. 4.7.

Here, the resistance was significantly reduced by a factor of about 2.4, allowing for much more bleeder current, without exceeding or closely approaching the on-board resistors' power rating. Also, the voltage division was designed to be relatively "flat" (Fig. 4.8) across stages from D1 to A, which is stated to be recommended for optimal gain.

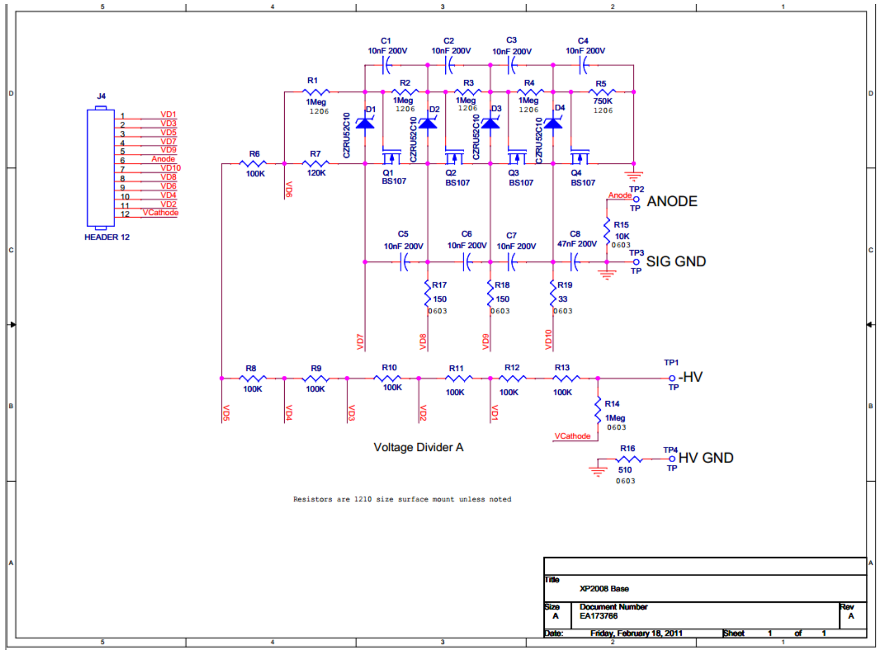

Figure 4.7: The Prototype v1 board circuit diagram received from Sten Hansen. The parts denoted with a Q are the MOSFET transistors, and the parts denoted with a D are the zener diodes. [8]

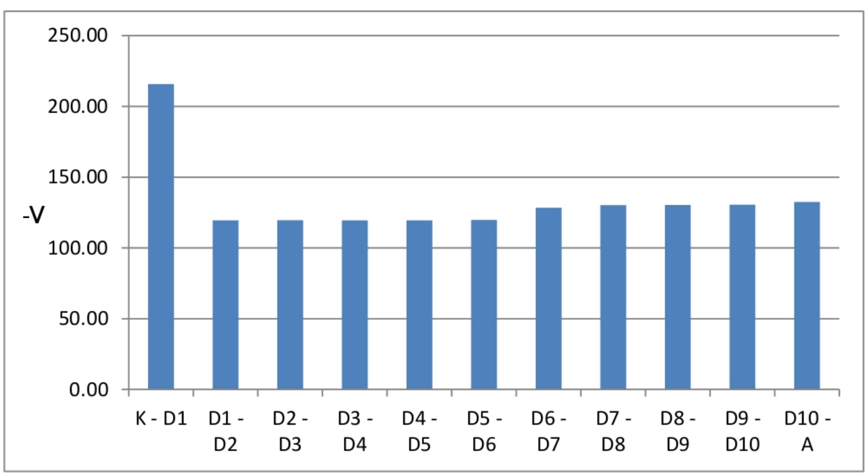

Figure 4.8: The voltage devision between subsequent stages for the Prototypes v1, v2, and v3 PMT base designs.

4.2.3 Prototype Base v2

The first modification made to the prototype board was to simply halve the resistance of each of the first six stages (R6-R13 on Fig. 4.7) to increase the bleeder current.

4.2.4 Prototype Base v3

This modification "transistorized" the D5-D6 and D6-D7 stages in the case that the destabilization was occurring even at these earlier stages (Figure 4.9).

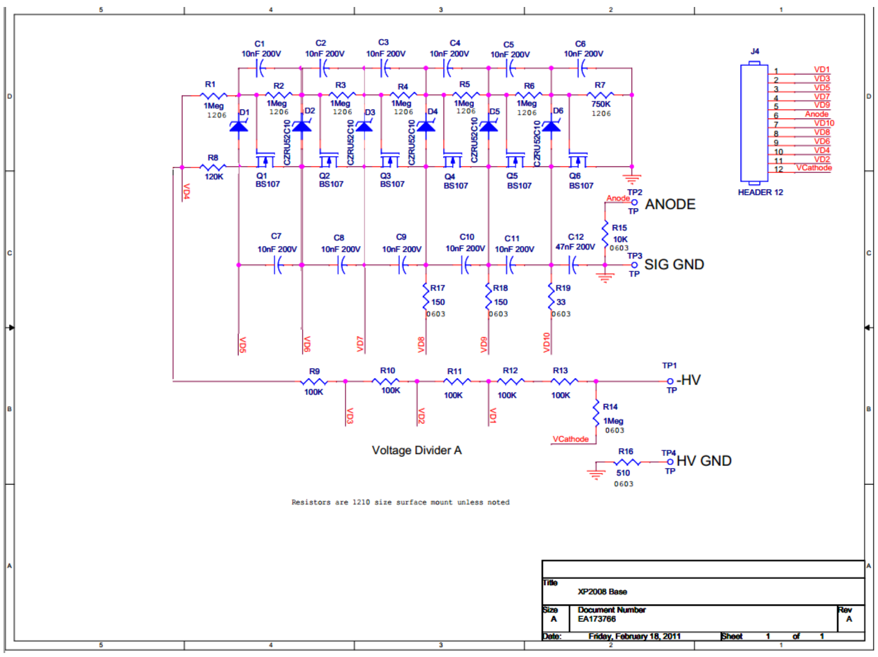

Figure 4.9: The Prototype v3 board: 3 more transistorized stages than the Prototype v1 design.

4.2.5 Prototype Base v4

Here, the resistance over the final stage (D10-A) was increased from $1M\Omega$ to $1.5M\Omega$ (R5 in Figure 4.7). This was done in case that the final batch of electrons needed help being "swept" to the anode with a higher voltage difference.

4.3 PMT Base Comparisons

There is a specific difficulty with the objective to increase the rate capability of our PMT's. This difficulty is that we do not have a target rate to attain. The rate and intensity that caused the original PMT+base

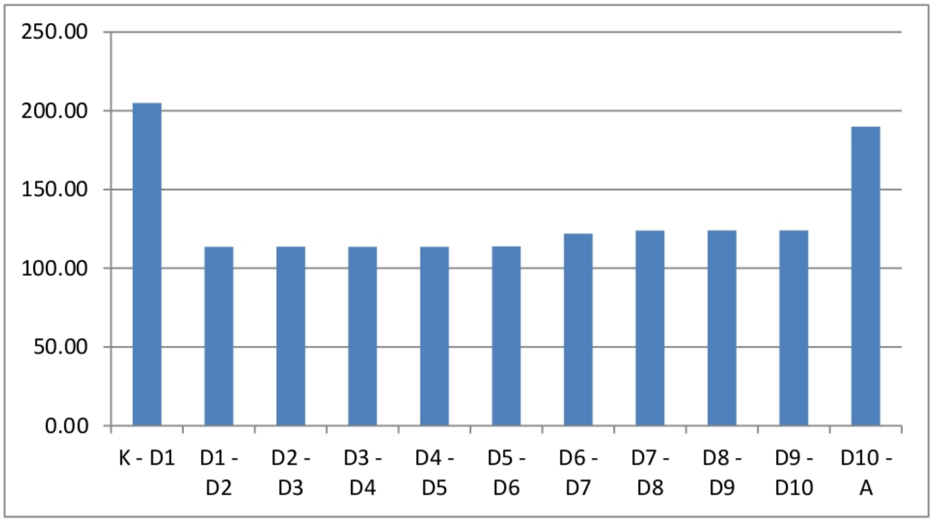

Figure 4.10: The (negative) voltage between subsequent stages for the Prototype v4 PMT base.

to sag is unknown, and if it was known, it would be difficult to match the intensity with an experimental setup.

As a result, the objective in these tests is to *compare* the performance of the same PMT using different bases.

4.3.1 Testing Apparatus and Measurments

In this experiment, a PMT attached to a PMT base is placed into a light-tight box along with an fast-pulsing LED.

The LED is driven by an Agilent function generator capable of generating signals up to 30MHz. The LED's intensity is attenuated by a neutral density filter (NDF), with a rating D=3.0, where the NDF allows 1 in 10^D photons through (1 in 1000 for D=3.0).

The PMT base is powered by a high voltage supply with an ammeter between the two in order to measure the bleeder current. The PMT signal is processed

Figure 4.11: Inside of a lightbox, we have our prototype board (left) wired up to a Philips XP-2008 PMT (middle), facing a fast-led source (right)

Chapter 5

Data Productions

5.1 Production Processing

The three raw outputs of the data acquisition systems, as described above are (1) Main DAQ CODA files, (2) Scaler DAQ CODA files, and (3) Beam DAQ ASCII files.

Each raw data file corresponds to the data taken from certain subsystems over approximately one to two hours of running time. These three types require varying degrees of de-serialization, parsing, processing, and storage – a process as a whole defined as *decoding*.

All raw data files are backed up to long-term tape storage (managed by FNAL Computing Division), and the decoded and processed data gets stored on one of four MySQL servers to be used for analysis by the collaboration. Data is also output to a ROOT file for the ease of use of one of the two independent tracking programs.

Contiguous blocks of decoded and tracked data is then grouped together into *merged* productions, available on all MySQL servers, providing collaborators large sets of curated and easily analyzable data.

5.1.1 Decoding Raw Data

The CODA file decoding is nearly identical for MainDAQ and ScalerDAQ, and only differ by content; the MainDAQ contains TDC readout. For each one to two hour *Run*, the CODA files can be well-described as the following sequence of events (and the data they contain):

1. Prestart Event (Run data)

2. Begin Spill Event (Spill data, Scaler readout)

3. Many Physics Events (Event data, TDC readout)

4. End Spill Event (Spill data, Scaler readout)

5. SlowControl Event (Slow control readout, Spill ID readout)

6. Spill Counter Event (Spill ID readout)

   ...(Repeat 2-6 for each *Spill*)

7. End Event

Our decoding program uses C and C++ in conjunction with Jefferson Lab's CODA I/O library to read these events and parse them according to their individual formats. Data from these CODA events are decoded and placed into hierarchical categories.

Run Level Data

Run-level data contains data and metadata pertaining to the entirety of the run that is recorded. At the time of the Prestart Event, the date and time of the run are stored, along with a readout of the specific settings of all non-trigger TDC boards.

After the End Event is encountered, metadata is aggregated and stored regarding such items as the number of chamber hits, the triggers that were fired, the target positions used, average magnet currents, and other useful metrics.

Spill Level Data

The *Beginning of Spill* (BOS) and *End of Spill* (EOS) events bookend the set of physics events for a given spill. At each BOS and EOS events, the 140 MHz VME scalers are read out. At the beginning of the spill, all scalers should be zeroed out, and then read out again after the spill has ended.

Slow Control events are read out between spills, which contain data regarding the current spill identifier number, target systems, beam and radiation monitors, and environmental readings.

The spill identifier (*spillID*) is what is used to synchronize the data together across various data acquisition systems. As such, the *spillID* is read out redundantly in both Slow Control and Spill Counter events (which contain only the *spillID* value) to ensure that the data is appropriately labeled.

When the End Event is reached, the independently-recorded Beam DAQ data (recorded in an ASCII file) is read and stored with the rest of the Spill-level data.

Event Level Data

For each spill, $\sim 3k$ events are triggered to be recorded. With each event, three types of information is stored: the trigger which fired the event, a measure of the beam intensity per RF bucket, and the full detector readouts. The detector readouts require the most processing of all the rest of the data. The CODA files contain the hardware addresses of each detector *hit*, along with a *TDC time*. The following steps briefly summarize the processing steps:

1. Mapping: Map the hardware address to a detector name and detector element number
2. Timing: Classify hits as in-time or not and calculate *drift time* from TDC time
3. R-T (time-to-space): Translate *drift time* to *drift distance*
4. After-Pulse Elimination: Remove hits that result from signal reflection and other electronic artefacts
5. Trigger Road Reconstruction: Use *v1495* TDC hits to reconstruct possible trigger roads that may have fired
6. Hodoscope Masking: Remove drift chamber hits that have no adjacent hodoscope hit
7. Trigger Road Masking: Same as hodoscope masking, but only using hodoscopes from reconstructed trigger roads

This fully processed data is then stored into one the experiment's MySQL databases.

5.2 Online and Offline Processing

There are two modes of productions: on-line and off-line productions. For on-line productions, all Run- and Spill-level data is decoded, but only 1-in-n Physics Events are processed, where n is typically 15. This *"sampling mode"* is used in order for the decoding to reliably keep up with even high-intensity beam data.

For off-line productions, a large group of categorically similar runs is defined, and the chain of production processing is initiated. The steps of this process is generally emphdecoding, tracking, archiving, and merging.

The decoding and tracking is performed on Fermilab Computing Service's FermiGrid, which provides the computing resources necessary to process hundreds of runs simultaneously.

A single decoding job submission will output the processed data to one of the four available MySQL servers and also to a ROOT file. Then, one job will be submitted to run one of the two tracking programs on the ROOT file, while another job is submitted to run the other tracking program on the MySQL data.

Once the tracking is completed, the ROOT file and the *Hit* table from the MySQL production is archived on the Fermilab BlueArc NAS backup system for future use, if necessary.

Upon the completion of decoding and tracking of a specified range of runs, all of their Run-, Spill-, and Event-level data, along with its tracked data, is combined into a single *merged* schema. These *merged* schemas are mirrored across all four of the MySQL servers for optimal redundancy and availability.

5.3 RDBMS Data Structure

The processed data is primarily stored in MySQL Server 5.1 databases. MySQL is an open-source **R**elational **D**ata**b**ase **M**anagement **S**ystem (RDBMS) developed by Oracle that is well-suited for the storage and responsive querying of hierarchical data.

Each run is decoded into its own schema, and contains its own instances of all tables of a specified design. The tables are all *join*-able to each other by sharing *foreign keys* with each other in the form of the *runID*'s, *spillID*'s, and *eventID*'s. The contents of the tables are *indexed* in such a way that *joins* and queries gain a speed performance boost, but this comes at the cost of disk space.

The data on the server is world-wide accessible and can be queried using the standard querying language. The queried data can be directed to any analysis code in any programming language due to the large array of MySQL API's available.

5.4 Data Quality

Chapter 6

Analysis

6.1 Particle Identification

6.2 Data Selection

6.2.1 Spill Level Cuts

Duty Factor

The beam structure is delivered in *bunches* of protons separated by 18.9ns. These bunches are better known as *RF buckets*, as they are synchronized with the 18.9ns cycle of the Fermilab RF clock. Ideally, each of these RF buckets deliver a steady number of protons per bucket.

In practice however, this is not the case, and not all the RF buckets delivered are occupied within a given spill. The fraction of buckets occupied is known as the accelerator Duty Factor, *DF*, and can be measured using a reference beam counter as

$$DF = \frac{\langle I \rangle^2}{\langle I^2 \rangle} \quad with \quad I = \sum_{N_t rig} N_{X2T} \tag{6.1}$$

where $N_X 2T$ is the number of hits in the X2T

Bin#	x_2 Range
0	(0.08, 0.14]
1	(0.14, 0.16]
2	(0.16, 0.18]
3	(0.18, 0.21]
4	(0.21, 0.25]
5	(0.25, 0.31]
6	(0.31, 0.53]

Table 6.1: x_2 bin ranges

target	yield
None	104
Empty	84
LH2	3138
LD2	3472
C	1721
Fe	1370
W	1553

Table 6.2: Raw dimuon yields for Roadset 57

6.2.2 Dimuon Level Cuts

6.2.3 Track Level Cuta

6.2.4 Other Cuts

6.3 Dimuon Yields

6.3.1 Binning of Data

The x_2 bins for this EMC ratio measurement were chosen such that each bin in x_2 has similar levels of statistics.

Concurrent with this analysis, studies of $\bar{d}(x_2)/\bar{u}(x_2)$ and parton energy loss are conducted. Due to the nearly identical source of signal across these studies (good Drell-Yan target dimuons), a consistent selection of kinematic binning maintains a certain continuity among analyses. The x_2 binning chosen can be found in Table 6.1

6.3.2 Raw Yields

The total number of target Drell-Yan events recorded for each target can be found in Table 6.2. The number of events broken down into

6.4 Rate Dependence and Combinatorial Background Correction

6.5 Empty/None Target Background Subtraction

6.6 Dimuon Yield Ratios

6.7 ld_2 Contamination Correction

6.8 Isoscalar Corrections for ^{183}W and ^{56}Fe

Chapter 7

Results

Chapter 8

Discussion

Chapter 9

Conclusions

We conclude that Bryan Dannowitz likes coffee.

Appendix A

PMT Upgrades

A.1 ARGUS PMT Performance 'Sag'

A.2 Prototype Testing

A.3 Manufacturing and Installation

Appendix B

MySQL Production Structure

B.1 MySQL Servers

B.2 Atomic Schema Design

B.3 Merged Schemas

References

[1] A. Alavi-Harati, T. Alexopoulos, M. Arenton, K. Arisaka, S. Averitte, R. F. Barbosa, A. R. Barker, M. Barrio, L. Bellantoni, A. Bellavance, J. Belz, D. R. Bergman, E. Blucher, G. J. Bock, C. Bown, S. Bright, E. Cheu, S. Childress, R. Coleman, M. D. Corcoran, G. Corti, B. Cox, A. R. Erwin, R. Ford, A. Glazov, A. Golossanov, G. Graham, J. Graham, E. Halkiadakis, J. Hamm, K. Hanagaki, Y. B. Hsiung, V. Jejer, D. A. Jensen, R. Kessler, H. G. E. Kobrak, J. LaDue, A. Lath, A. Ledovskoy, P. L. McBride, P. Mikelsons, E. Monnier, T. Nakaya, K. S. Nelson, H. Nguyen, V. O'Dell, M. Pang, R. Pordes, V. Prasad, X. R. Qi, B. Quinn, E. J. Ramberg, R. E. Ray, A. Roodman, S. Schnetzer, K. Senyo, P. Shanahan, P. S. Shawhan, J. Shields, W. Slater, N. Solomey, S. V. Somalwar, R. L. Stone, E. C. Swallow, S. A. Taegar, R. J. Tesarek, G. B. Thomson, P. A. Toale, A. Tripathi, R. Tschirhart, S. E. Turner, Y. W. Wah, J. Wang, H. B. White, J. Whitmore, B. Winstein, R. Winston, T. Yamanaka, and E. D. Zimmerman. Measurements of direct CP violation, CPT symmetry, and other parameters in the neutral kaon system. *Phys. Rev. D*, 67:012005, Jan 2003.

[2] J.J. Aubert et al. The ratio of the nucleon structure functions $F2_n$ for iron and deuterium. *Phys.Lett.*, B123:275, 1983.

[3] CAEN. v1495 general purpose vme board. `http://www.caen.it/csite/CaenProd.jsp?idmod=484&parent=11`. Accessed: 2016-01-26.

[4] S. D. Drell and Tung-Mow Yan. Massive Lepton Pair Production in Hadron-Hadron Collisions at High-Energies. *Phys. Rev. Lett.*, 25:316–320, 1970. [Erratum-ibid.25:902,1970].

[5] Chun-Gui Duan, Na Liu, and Zhan-Yuan Yan. The extraction of nuclear sea quark distribution and energy loss effect in drell-yan experiment. *EUR.PHYS.J.C*, 50:585, 2007.

[6] I. Estermann, R. Frisch, and O. Stern. Magnetic Moment of the Proton. *Nature*, 132:169–170, jul 1933.

[7] Donald F. Geesaman, K. Saito, and Anthony William Thomas. The nuclear EMC effect. *Ann.Rev.Nucl.Part.Sci.*, 45:337–390, 1995.

[8] Sten Hansen. private communication, 2012.

[9] E. A. Hawker et al. Measurement of the light antiquark flavor asymmetry in the nucleon sea. *Phys. Rev. Lett.*, 80:3715–3718, Apr 1998.

[10] C. R. Kerns. A High Rate Phototube Base. *IEEE Trans. Nucl. Sci.*, 24:353–355, 1977.

[11] G. Moreno, C. N. Brown, W. E. Cooper, D. Finley, Y. B. Hsiung, A. M. Jonckheere, H. Jostlein, D. M. Kaplan, L. M. Lederman, Y. Hemmi, K. Imai, K. Miyake, T. Nakamura, N. Sasao, N. Tamura, T. Yoshida, A. Maki, Y. Sakai, R. Gray, K. B. Luk, J. P. Rutherfoord, P. B. Straub, R. W. Williams, K. K. Young, M. R. Adams, H. Glass, and D. Jaffe. Dimuon production in proton-copper collisions at $\sqrt{s} = 38.8$ gev. *Phys. Rev. D*, 43(9):2815–2835, May 1991.

[12] MVME. Mvme5500 series vmebus single-board computer. `http://www.mvme.com/manuals/MVME5500e-SPEC.pdf`. Accessed: 2016-01-26.

[13] Brews Ohare. Mosfet structure. https://commons.wikimedia.org/wiki/File:MOSFET_Structure.png, March 2012. Accessed: 2016-02-01.

[14] HCZ Photonics. Xp2072: High energy resolution , 10-stage, 39mm (1.5") tube. http://hzcphotonics.com/products/XP2072.PDF. Accessed: 2016-01-29.

[15] J. Pumplin et al. New generation of parton distributions with uncertainties from global QCD analysis. *JHEP*, 07:012, 2002.

[16] J. Seely et al. New measurements of the EMC effect in very light nuclei. *Phys. Rev. Lett.*, 103:202301, 2009.

[17] Shiuan-Hal Shiu, Jinyuan Wu, Randall Evan McClellan, Ting-Hua Chang, Wen-Chen Chang, Yen-Chu Chen, Ron Gilman, Kenichi Nakano, Jen-Chieh Peng, and Su-Yin Wang. FPGA-based trigger system for the Fermilab SeaQuest experiment. *Nucl. Instrum. Meth.*, A802:82–88, 2015.

[18] R. S. Towell et al. Improved measurement of the anti-d/anti-u asymmetry in the nucleon sea. *Phys. Rev.*, D64:052002, 2001.

[19] T. Zimmerman and J. Hoff. The design of a charge integrating, modified floating point ADC chip. *IEEE J. Solid State Circuits*, 39:895–905, 2004.